An elastic wedge model for the development of coeval normal and thrust faulting in the Mauna Loa-Kilauea rift system in Hawaii

An Yin and T. K. Kelty

Department of Earth and Space Sciences and Institute of Geophysics and Planetary Physics
University of California, Los Angeles

Abstract. A long-standing enigma of the Mauna Loa-Kilauea rift system in Hawaii is the coeval development of normal and thrust faults that are vertically partitioned. To address this question, we developed a simple elastic wedge model that explores plausible boundary conditions in terms of tractions for generating such a fault pattern. Analytical solutions that best simulate the observed faulting style and geodetically determined strain at the surface require that (1) the pore fluid pressure ratio within the wedge (λ) and along the basal decollement (λ_b) must be exceedingly high (i.e., $\lambda = \lambda_b = 0.90$-$0.95$) and (2) a tensile stress of the order of 10-30 MPa must have existed in the very top part of the rift zone at the back side of the wedge-shaped rift flank. The high pore fluid pressure within the rift flank may be induced by pumping of fluids during emplacement of magma, whereas the high pore fluid pressure along the basal decollement may be caused by compaction of water-saturated sediments between the volcanic pile above and the oceanic floor below. Although the predicted tensile stress in the rift zone could be related to the presence of a relatively steep topographic slope, our results show that this is not a prerequisite. Therefore we attribute occurrence of tensile stress to either upward bending of the Hawaiian volcanic pile due to emplacement of magma, or inflation of a shallow magma chamber several kilometers beneath the surface. In any case, the results of our model indicate that magma emplacement in the shallow part of the rift zone may be a passive process, while the deep rift zone experiences forceful emplacement (i.e., active rifting via magma push).

1. Introduction

The development of the Hawaiian volcanic island chain has long been recognized as a result of the Pacific plate moving over a hotspot [*Clague and Dalrymple*, 1987]. However, processes associated with interaction between the upwelling of mantle materials and their final emplacement at crustal levels remain poorly understood. One of the critical issues is under what mechanical conditions the volcanic chain has maintained its continued growth [e.g., *Fiske and Jackson*, 1972]. For example, it is not clear whether the volcano construction has been accomplished purely by eruption or by a significant amount of magmatic intrusion [*DePaolo and Stolper*, 1996; cf. *Borgia*, 1994; *Borgia and Treves*, 1992; *Dieterich*, 1988; *Iversion*, 1995]. To address this question, extensive geologic and geophysical investigations have been conducted which focused on the relationship between the magmatic activity and deformation pattern in the active Mauna Loa-Kilauea rift system on the island of Hawaii (Figure 1) [e.g., *Lipman et al.*, 1985; *Decker et al.*, 1987; *Denlinger and Okubo*, 1995; *Wallace and Delaney*, 1995; *Gillard et al.*, 1996; *Delaney et al.*, 1998]. A puzzling result from these studies is the discovery of mixed modes of deformation in the rift flank, that is, thrust, normal, and decollement-type faulting all occurred synchronously [*Lipman*, 1980; *Lipman et al.*, 1985; *Wyss*, 1988; *Wyss et al.*, 1992 a, b; *Gillard et al.*, 1996]. Field mapping shows that surface deformation of the Mauna Loa-Kilauea rift system is dominated

by normal faults [e.g., *Lipman*, 1980; *Lipman et al.*, 1985] (Figure 1a). However, focal mechanism studies of earthquakes suggest that the dominant seismic energy (>80%) has been released by thrust faulting [*Gillard et al.*, 1996]. These observations, when considered together, strongly imply that deformation in the rift system has been partitioned vertically: normal faulting in the shallow part and thrust faulting in the deep part of the rift flank (Figure 1b).

Directly related to this observation of coeval normal and thrust faulting is how the magmatic activity interacts with deformation in the rift flank in the Mauna Loa-Kilauea rift system. *Moore and Krivoy* [1964] were among the first to consider the dynamics of the rift system and to suggest that gravitational slumping was the major factor causing the rift to open and widen, allowing magma to move passively into fractures near the breakaway of the slumping block. In contrast, *Swanson et al.* [1976] propose that magmatic pressure pushes the rift apart and slumping is a result rather than the cause of rifting. As both driving mechanisms are mechanically feasible [*Dieterich*, 1988; cf. *Iverson*, 1995], early workers have postulated two drastically different fault patterns on cross section for the structures in the rift flank (see Figures 1b and 1c). More recently, *Clague and Delinger* [1994] propose that spreading of dunite cumulate in the rift zone may be the cause for seaward motion and deformation of the rift flank.

Geodetic surveys in the past few decades in the island of Hawaii have provided a wealth of data on active deformation of the rift system [e.g., *Davis*, 1986; *Yang et al.*, 1988, 1992; *Delaney et al.*, 1990, 1993, 1998; *Wallace and Delaney*, 1995; *Owen et al.*, 1995]. For example, *Delaney et al.* [1998] examined systematically the seismic, triangulation, leveling, ground surface tilt, and
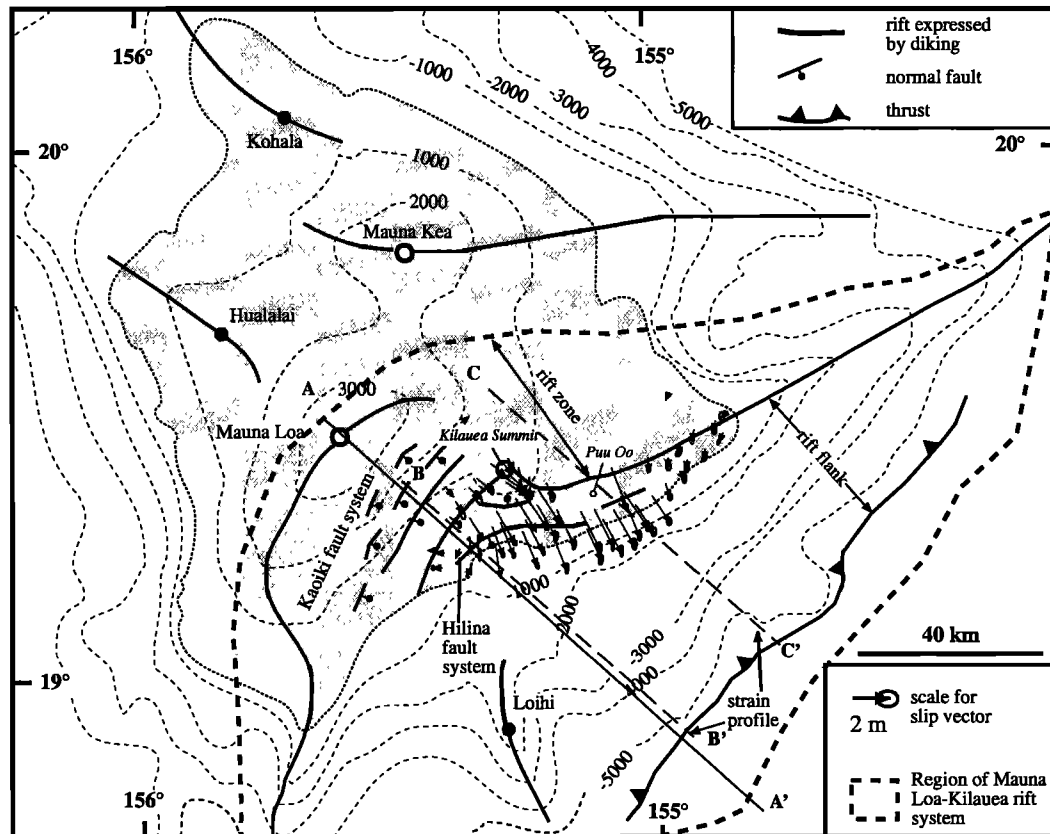
Figure 1. (a) (opposite) Tectonic map of the Mauna Loa-Kilauea rift system. The rift system is divided into a rift zone where formation of dikes is the dominant mode of deformation and a rift flank where both normal and thrust faulting occurs. AA' is the location of cross sections shown in Figures 1b and 1c. Vectors shown on the map are geodetically determined, horizontal displacements from *Delaney et al.* [1998]. Displacement vectors in the region between lines of BB' and CC' were first projected into a single cross section; their horizontal gradient along the profile direction was then calculated to provide the estimates of the horizontal strain distribution at the surface as shown in Figure 2a. (b) A possible cross section of the south flank of the Mauna Loa-Kilauea rift system. Normal faults occupy the upper part of the wedge-shaped rift system, whereas thrusts occupy the lower part of the rift system, modified after *Hill and Zucca* [1987], *Moore et al.* [1995], and *Gillard et al.* [1996]. The active conduits are solid. Implied state of stress immediately against the rift zone by this cross section is also shown, where S1 and S3 are the greatest and least compressive stresses, respectively. S1 is vertical near the surface but rotates 90° to the horizontal direction near the deeper part of the rift zone. (c) An alternative cross section of the south flank of the Mauna Loa-Kilauea rift system showing that the wedge is completely occupied by normal faults. These faults extend to the base of the wedge and are connected with the basal thrust decollement, modified after *Lipman et al.* [1985] and *Okubo et al.* [1997]. This cross section implies that S1 is vertical along the entire depth of the rift zone.

GPS data collected in the Kilauea region and found that the Kilauea summit has experienced continuous subsidence while its rift flank has been uplifted since 1976. Horizontal extension has also occurred with its rate decreasing from >25 cm yr^{-1} in 1983 to < 5 cm yr^{-1} in 1996. Although the displacement field varies with time, it does not mean that the corresponding strain field must vary with time because strain is measured by the spatial gradient of displacement. That is, if we increase the displacement vector at two points for the same amount (say Δu) at a particular time window from some initial displacement value of u_1 and u_2 at each point, respectively, then the strain between the two points remains the same. Thus an overall decrease in the magnitude of displacement in the rift system may simply indicate that the entire rift flank was translated as a rigid block at a decreasing rate. We use the horizontal displacement vectors of *Delaney et al.* [1998] (Figure 1a) to calculate the distribution of the horizontal strain in the N45°W-S45°E direction (Figure 2a), which shows that the

linear strain in the horizontal direction is extensional, and its magnitude decreases systematically southeastward away from the rift zone.

The geodetically determined deformation field also provides constraints on the kinematic relationship between magma transport and deformation in the Mauna Loa-Kilauea rift system. *Wallace and Delaney* [1995] and *Owen et al.* [1995] suggest that the surface displacement field of the Kilauea volcanic system may be explained by a combination of both emplacement of steeply dipping dikes in the rift zone and slip along a low-angle thrust at the base of the rift flank. Because these models are purely kinematic in a sense that their boundary conditions involve no prescribed tractions, little has been learned regarding conditions of forces under which the rift system has been deformed.

Concerned with the stress distribution in the Mauna Loa-Kilauea rift system, *Thurber and Gripp* [1988] suggest that the wedge-shaped rift flank and the associated normal faults may be
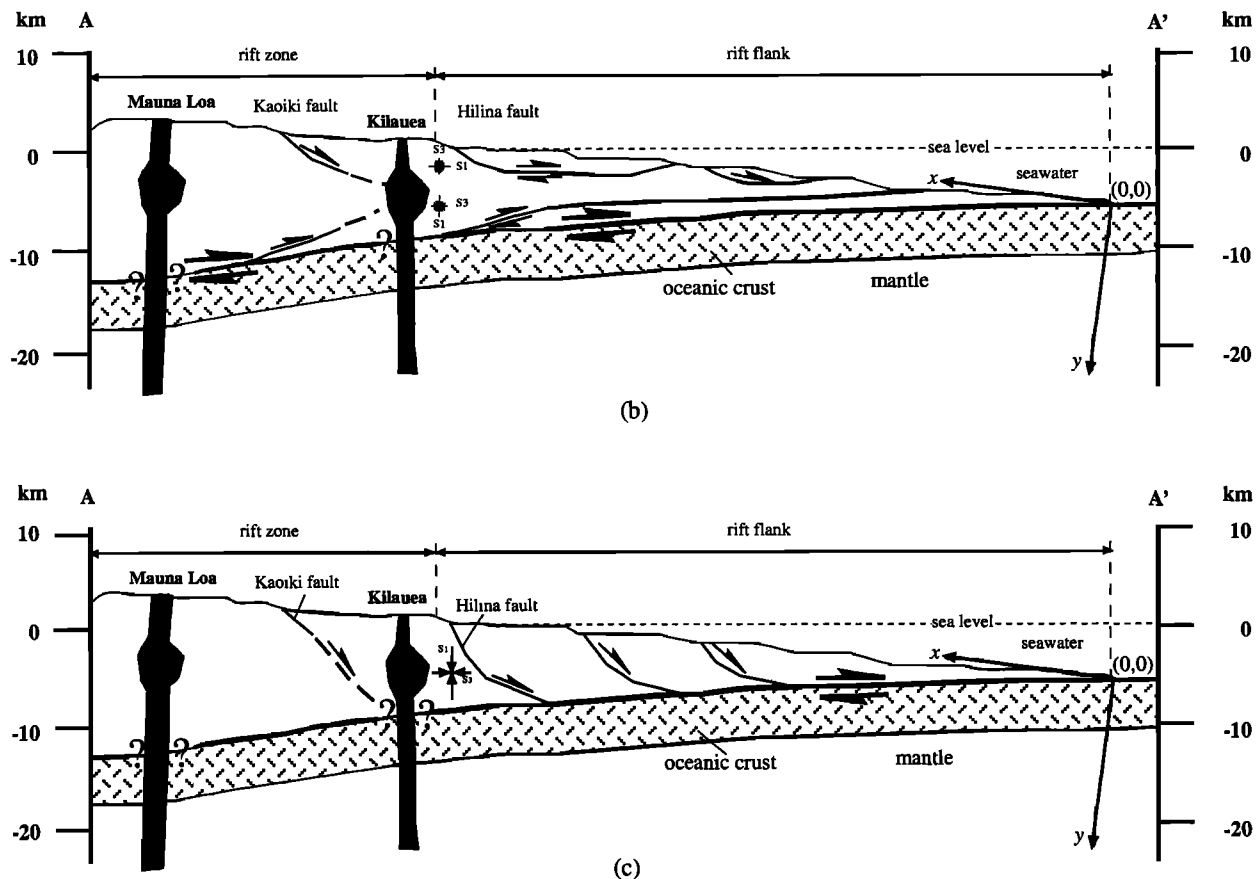
(b)

(c)

Figure 1. (continued)

explained by the noncohesive critical Coulomb wedge model of *Davis et al.* [1983] and *Dahlen* [1984]. Their interpretation is problematic because the Coulomb wedge model predicts that either the wedge is occupied completely by thrusts or normal faults, but not both at the same time. Using a finite element code of *Melosh and Raefsky* [1980] and *Melosh and Williams* [1989], *Borgia* [1994] investigated the long-term effect of stress distribution in the Mauna Loa-Kilauea rift system. This model considers a two-dimensional triangular volcanic complex that rests on top of an elastic layer representing the oceanic lithosphere. The elastic layer is in turn underlain by an inviscid fluid representing the asthenosphere. The volcanic complex consists of two parts: (1) a "low" viscous nucleus representing an intrusive complex and (2) a "high" viscous region representing the rift flank. When the model was suddenly loaded by the weight of an intrusive complex, the system is first dominated by strong horizontal compression in the upper part of the rift system, probably induced by downward bending of the elastic plate [see *Borgia,* 1994, Plate 5]. *Borgia* [1994] finds that only when this low viscosity region relaxes or spreads for thousands of years can extension be produced in the shallow part of the rift flank with coeval but much weaker horizontal compression in the deeper rift flank [see *Borgia,* 1994, Plate 6]. If magmatic intrusion in the Mauna Loa-Kilauea rift system is episodic and the effect of its loading is as "sudden" as envisioned by the Borgia model, then a natural prediction of the model is that the development of thrusts and normal faults in the upper rift system should have alternated. That is, thrusts develop during the sudden emplacement of an intrusive complex, while normal faults occur during the spreading stage of the intrusive complex. However, such a predicted link between episodic

magma emplacement and alternating development of thrust and normal faults has not been documented in the geologic record of the Mauna Loa-Kilauea rift system.

2. Elastic Wedge Model

The obvious difference in the predicted state of stress between the magmatic push and gravitational sliding models in and near the rift zone highlights the need for understanding boundary conditions exerted by magmatic activity toward the rift flank. However, owing to the lack of seismicity in the deeper part of the rift zone [*Gillard et al.*, 1996], this has been a difficult task. To resolve this problem, we explore possible mechanical causes for the occurrence of coeval normal and thrust faulting in the south rift flank of the Mauna Loa-Kilauea rift system. We take an inverse problem approach to search for plausible traction conditions in the rift zone using simple elastic solutions. That is, we assume a polynomial form of Airy stress function [*Fung,* 1965] satisfying partially defined boundary conditions at the top, base, and the back of the rift flank as the elastic solution of the problem. By selecting the solution that predicts the observed stress and strain distributions, we simultaneously determine the possible traction conditions in the rift zone. Although the solution of the problem obtained by this approach is not unique, because the boundary conditions are incompletely defined, they help provide possible mechanical conditions under which the Mauna Loa-Kilauea rift system has been developed. The specific predictions of the solutions can also be systematically tested by future stress and strain measurements from the rift system.

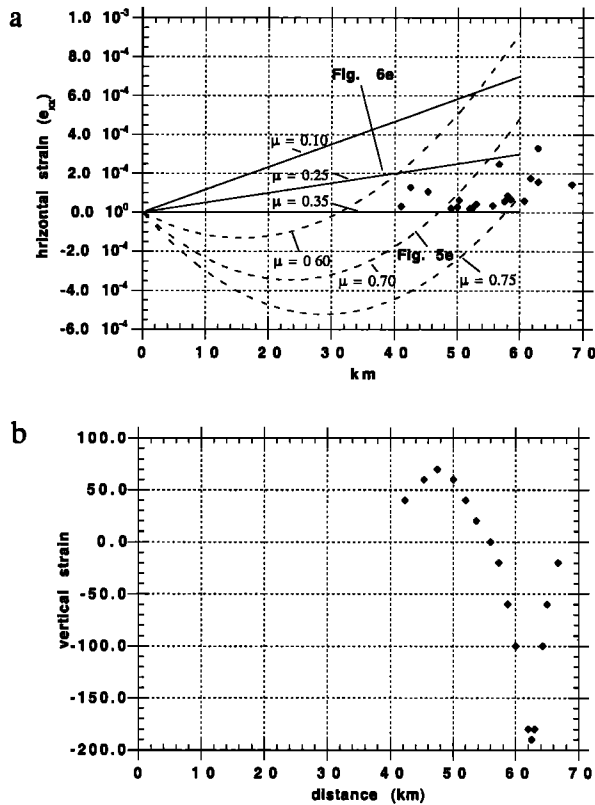The model presented in this study follows the earlier work of

a

b

Figure 2. (a) Points on the diagram represent horizontal strain at the surface calculated from the displacement vectors of *Delaney et al.* [1998] in the region between lines BB' and CC' shown in Figure 1. Uncertainties are not shown as they are much smaller (on average of the order of 10^{-4} or less) than the range of scattering of the strain data. Note that the horizontal axis is measured from the toe of the rift flank toward the rift zone. Though highly scattered, the horizontal strain is extensional and its magnitude decreases from the rift zone toward the toe of the rift flank. The lack of strain data for the submarine portion of the rift flank precludes determination of whether the horizontal strain component varies linearly or nonlinearly from the toe to the rift zone. The straight lines represent linear solutions (i.e., $\alpha_0 = 0.0$) with varying coefficients of basal friction $\mu_b = 0.10$, 0.25, and 0.35, whereas curves represent non-linear solutions (i.e., $\alpha_0 = -0.05$) with varying coefficients of basal friction $\mu_b = 0.60$, 0.70, and 0.75. Lines labeled with Fig. 5e and Fig. 6e are the predicted horizontal strain distributions at the surface derived from the solutions shown in Figures 5e and 6e (see text), respectively. (b) A profile showing the horizontal distribution of the vertical displacement along the BB' section (see Figure 1a for location). The lack of information on vertical distribution of the vertical displacement precludes calculation of vertical strain. Data are from *Delaney et al.* [1998].

Yin [1993]. However, several key differences exist between the two studies. For example, the solution obtained by *Yin* [1993] is valid only for a special situation, that is, Amonton's law is satisfied only at one point along the base of the wedge. However, this limitation can be easily removed as we show in the following derivation. In addition to this difference, the approach presented below uses the magmatic pressure in the rift zone as an incomplete boundary condition at the back of the wedge and at the same time considers the effect of water load on top of the elastic wedge. Finally, a more general, nonlinear form of stress distribu-

tion as a function of spatial coordinates x and y is considered. This expansion of the solution from the special case of *Yin* [1993] allows a general treatment of possibly varying magmatic densities at the back of the wedge.

2.1. Geometry of the Wedge and Governing Equations

Following the interpretation of *Ando* [1979], *Nakamura* [1980], *Hill and Zucca* [1987], and *Wyss* [1988], we assume that the basal decollement dips at a shallow angle towards the rift zone in the Mauna Loa-Kilauea region. Therefore the rift system may be approximated as a wedge-shaped block in cross section (Figures 1b, 1c, and 3). The deformation we intend to simulate is that of the rift flank (Figure 1), where deformation is prominently expressed by release of seismic (elastic) energy. A region of viscous deformation may exist in the rift zone within a few kilometers near volcanic centers and magmatic chambers (Figure 3), suppressing seismicity [e.g., *Delaney et al.*, 1998].

The geometry of the wedge, the framework of reference, and key model parameters are shown in Figure 3. In the calculation, tensile stress is positive, and pressure (compressive) is negative. We assume that the Mauna Loa-Kilauea rift flank behaves as a homogeneous, isotropic, porous elastic medium with a uniform density and a constant pore fluid pressure gradient in the vertical direction. Under these assumptions the stress equilibrium equations in the x and y directions for a plane strain condition may be written as

$$\frac{\partial \bar{\sigma}_{xx}}{\partial x} + \frac{\partial \sigma_{xy}}{\partial y} + X_e = 0 \tag{1}$$

$$\frac{\partial \sigma_{xy}}{\partial x} + \frac{\partial \bar{\sigma}_{yy}}{\partial y} + Y_e = 0, \tag{2}$$

where $\bar{\sigma}_{xx} = \sigma_{xx} - P_f$ and $\bar{\sigma}_{yy} = \sigma_{yy} - P_f$ are the effective normal stress components in the x and y directions (P_f is the pore fluid pressure), σ_{xx}, σ_{yy}, and σ_{xy} are the normal and shear stress components, and X_e and Y_e are body forces induced by both gravity (F_g) and buoyancy of pore fluid (F_b) in the x and y directions (Figure 3). The body forces may be defined as

$$X_e = -(1-\lambda)\rho_w g \sin\alpha \tag{3a}$$

$$Y_e = (1-\lambda)\rho_w g \cos\alpha \tag{3b}$$

where ρ_w is the average rock density of the wedge, g is the gravitational acceleration, λ is the generalized Hubbert-Rubey pore fluid pressure ratio inside the wedge which is defined by [*Dahlen*, 1984]

$$\lambda = \frac{P_f + \rho_{H2O} g D}{P_L + \rho_{H2O} g D}, \tag{4}$$

where P_L is the generalized lithostatic pressure that includes loading induced by both rock inside the wedge and water overlying the wedge (i.e., $P_L = -\rho_w g z - \rho_{H2O} g D$), D is the depth of water overlying the wedge, and ρ_{H2O} is the density of the sea water (Figure 3). As discussed by *Hubbert and Rubey* [1959], the role of λ inside the wedge is to provide a body force pointing upward which counters the gravity that points downward. As a net result, the pore fluid pressure reduces the apparent density of the wedge. This effect is best explained in (3), in which the term
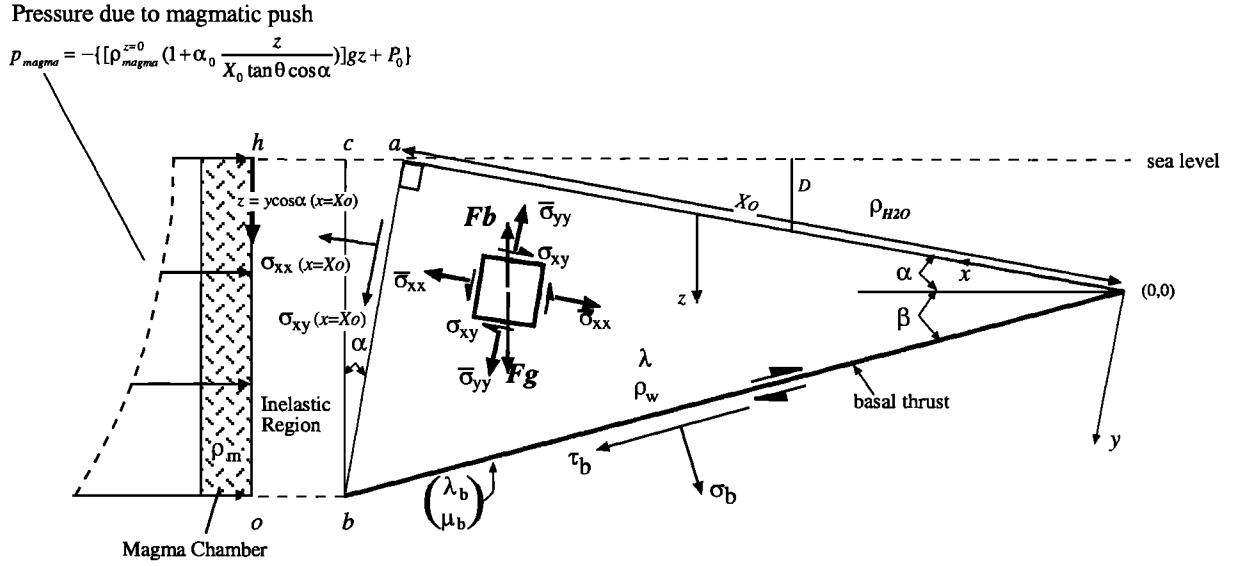
Pressure due to magmatic push

$$P_{magma} = -\{[\rho^{z=0}_{magma}(1+\alpha_0 \frac{z}{X_0\tan\theta\cos\alpha})]gz + P_0\}$$

Figure 3. Wedge geometry and framework of reference used in the model. Geometric and physical parameters used in the model are defined as follows: α is the surface slope; β is the dip of the basal thrust; σ_b and τ_b are normal and shear tractions on the basal thrust, respectively; $\sigma_{xx}(x = X_o)$ and $\sigma_{xy}(x = X_o)$ are normal and shear tractions on the back of the wedge; ρ_{magma}, ρ_w, and ρ_{H2O} are densities for magma, wedge, and overlying water; λ_b and λ are pore fluid pressure ratios along the basal thrust and within the wedge, respectively; μ_b is the coefficient of friction on the basal decollement. Body forces induced by gravity (Fg) and buoyancy of fluid pressure (Fb) are also shown.

$(1-\lambda)\rho_w$ may be viewed together as the effective density of the wedge. Thus, to change λ is to change the body force in the system, which in turn changes the state of stress without altering boundary conditions.

A general solution for the stress distribution in an elastic solid may be determined by the Airy stress function method [*Fung,* 1965]. We assume that the Airy stress function has the following form:

$$\Phi = \frac{1}{6}K_1x^3 + \frac{1}{2}K_2x^2y + \frac{1}{2}K_3xy^2 + \frac{1}{6}K_4y^3 + \frac{1}{6}K_5xy^3$$
$$+\frac{1}{6}K_6x^3y + \frac{1}{2}K_7x^2 + \frac{1}{2}K_8y^2 + K_9y^4 + K_{10}x^4$$
$$+K_{11}x^2y^2, \tag{5}$$

where K_1 to K_{11} are constants to be determined by the boundary conditions and Φ satisfies the biharmonic equation [*Fung,* 1965]

$$\nabla^4\Phi = \frac{\partial^4\Phi}{\partial x^4} + 2\frac{\partial^4\Phi}{\partial x^2\partial y^2} + \frac{\partial^4\Phi}{\partial y^4} = 0. \tag{6}$$

Substituting (5) into (6), we obtain

$$24K_{10} + 8K_{11} + 24K_9 = 0. \tag{7}$$

The Airy stress function Φ may be related to the normal and shear stress components in the x and y directions using [*Fung,* 1965]

$$\overline{\sigma}_{xx} = \frac{\partial^2\Phi}{\partial y^2} - X_ex = K_3x + K_4y + K_5xy + K_8$$
$$+12K_9y^2 + 2K_{11}x^2 - X_ex, \tag{8}$$

$$\overline{\sigma}_{yy} = \frac{\partial^2\Phi}{\partial x^2} - Y_ey = K_1x + K_2y + K_6xy + K_7$$
$$+12K_{10}x^2 + 2K_{11}y^2 - Y_ey, \tag{9}$$

$$\sigma_{xy} = -\frac{\partial^2\Phi}{\partial x\partial y} = -K_2x - K_3y - \frac{1}{2}K_5y^2 - \frac{1}{2}K_6x^2$$
$$-4K_{11}xy. \tag{10}$$

The particular solutions we are searching for are those that satisfy the boundary conditions at the base, the back, and the top of the wedge, through which constants K_1-K_{11} in (8)-(10) are to be determined.

2.2. Boundary Conditions on the Top of the Wedge

The boundary condition on the top of the wedge is defined by the load of the overlying seawater normal to the surface and zero shear stress parallel to the surface (i.e., assuming that viscosity of water is negligible). These conditions may be expressed as

$$\sigma_{yy}(x,0) = -\rho_{H2O}gL, \tag{11}$$

$$\sigma_{xy}(x,0) = 0. \tag{12}$$

Because the effective stress and the pore fluid pressure at the wedge top is $\overline{\sigma}_{yy}(x,0) = \sigma_{yy} - P_f$ and $P_f = -\rho_{H2O}gD$, respectively, the relationship shown in (11) implies that $\overline{\sigma}_{yy}(x,0) = 0$. Note that when the wedge is not overlain by water, such as the case of *Yin* [1993], $\overline{\sigma}_{yy}(x,0) = \sigma_{yy}(x,0) = 0$. Inserting $\overline{\sigma}_{yy}(x,0) = 0$ into (9) and (12) into (10), we determine the following constants

$$K_1 = 0, \tag{13}$$

$$K_2 = 0, \tag{14}$$

$$K_6 = 0, \tag{15}$$

$$K_7 = 0, \tag{16}$$

$$K_{10} = 0, \tag{17}$$

and using (17), equation (7) becomes

$$K_{11} = -3K_9. \tag{18}$$

2.3. Boundary Conditions Along the Base of the Wedge

The boundary condition along the base of the wedge is assumed to follow Amonton's law [*Jaeger and Cook*, 1979]

$$\tau_b(x, y = \tan\theta) = -\mu_b' \, \bar\sigma_b(x, y = \tan\theta), \tag{19}$$

where $\bar\sigma_b$ and μ_b are the effective normal and shear tractions in the wedge immediately above the base, respectively, and μ_b' is the effective coefficient of friction. The latter is defined by

$$\mu_b' = \mu_b \frac{(1-\lambda_b)}{(1-\lambda)}, \tag{20}$$

where λ_b is the pore fluid pressure ratio at the base of the wedge. The basal normal and shear tractions $\bar\sigma_b$ and τ_b can be related to effective normal and shear stress components at the base of the wedge in the x and y directions by

$$\bar\sigma_b = l^2\bar\sigma_{xx} + m^2\bar\sigma_{yy} + 2lm\sigma_{xy}, \tag{21a}$$

$$\tau_b = \sigma_{xy}(m^2 - l^2) + (\bar\sigma_{xx} - \bar\sigma_{yy})lm, \tag{21b}$$

where $l = -\sin\theta$ and $m = \cos\theta$. Inserting (21a) and (21b) into (19) leads to a simplified algebra equation

$$A\sigma_{xy} + B\bar\sigma_{yy} - C\bar\sigma_{xx} = 0, \tag{22}$$

where

$$A = l^2 - m^2 + 2\mu_b' l m, \tag{23}$$

$$B = l m + \mu_b' m^2, \tag{24}$$

$$C = l m - \mu_b' l^2. \tag{25}$$

Inserting (8), (9), and (10) into (22), we obtain an equation in the form of

$$a_0 x^2 + b_0 x + c_0 = 0, \tag{26}$$

where

$$a_0 = A(-\frac{1}{2}K_5\tan^2\theta + 12K_{11}\tan\theta) - B6K_9\tan^2\theta$$
$$-C(K_5\tan\theta + 12K_9\tan^2\theta - 6K_9), \tag{27}$$

$$b_0 = -AK_3\tan\theta - BY_e\tan\theta - C(K_3 + K_4\tan\theta - X_e), \tag{28}$$

$$c_0 = -CK_8. \tag{29}$$

In the most general case, the validity of (26) for any value of x requires that $a_0 = b_0 = c_0 = 0$. When $a_0 = 0$ and noting that $K_{11} = -3K_9$, the following relation may be derived from (27)

$$K_5 = TK_9, \tag{30}$$

where

$$T = \frac{12A\tan\theta - 12C\tan^2\theta + 6C - 6B\tan^2\theta}{(\frac{1}{2}A\tan\theta + C)\tan\theta}. \tag{31}$$

When $b_0 = 0$, equation (28) requires that

$$K_4 = K_3Q - S, \tag{32}$$

where

$$Q = -\left(\frac{A\tan\theta + C}{C\tan\theta}\right) \tag{33}$$

$$S = \frac{B Y_e - C X_e}{C\tan\theta}. \tag{34}$$

Finally, when $c_0 = 0$, equations (16) and (29) together yield

$$K_8 = 0. \tag{35}$$

The use of boundary conditions on the top and the base of the thrust wedge have left two constants, K_3 and K_9 in (5), undetermined. The required additional equations come from the boundary condition on the back of the wedge.

2.4. Boundary Conditions on the Back of the Wedge

As rifting and magmatic emplacement are the dominant processes in the rift zone, it is natural to assume that magmatic pressure provides a push at the back of the wedge [e.g., *Dieterich*, 1988]. This pressure may be a combination of the following terms: (1) a lithostatic pressure induced by the magma with an associated linear increase in density with depth due to differentiation of crystals according to their densities in the magmatic conduit, and (2) an excess pressure deviating from that of the lithostatic pressure [*Iverson*, 1995]. The combination of these effects can be expressed in (Figure 3)

$$P_{\text{magma}} = -\{[\rho_{\text{magma}}^{z=0}(1 + \alpha_0 \frac{z}{X_0\tan\theta\cos\alpha})]gz + P_0\}, \tag{36}$$

where ρ_{magma} is the total pressure at the back side of the wedge (i.e., $x = X_0$), $\rho_{\text{magma}}^{z=0}$ is the magma density at the surface, α_0 is a dimensionless constant measuring a fraction of the vertical gradient of magma density, and P_0 (positive when it is compressive) is an excess pressure deviating from the lithostatic pressure of magma. Note that the z axis points vertically down and is not parallel to the y axis. Its value can be related to y at the back of the wedge by $z = y\cos\alpha$ (Figure 3). When $\alpha_0 > 0$, the scheme of normlization shown in (36) indicates that the magma density at the base of the wedge in the rift zone is $\rho_{\text{magma}} = \rho_{\text{magma}}^{z=0}(1 + \alpha_0)$. For example, when α_0 is 0.1, the magma density at the bottom of the rift zone is $\rho_{\text{magma}} = \rho_{\text{magma}}^{z=0}(1 + 0.1) = 1.1\rho_{\text{magma}}^{z=0}$. When $\alpha_0 = 0$, the magma density is constant and the total magmatic pressure is a linear function of depth. Finally, when $\alpha_0 < 0$, it may be interpreted as a measure of an upward linear increase in tensile stress. Assigning a prescribed value for P_0 is problematic because it is not even clear whether it should be compressive or tensile. If P_0 is due to degassing of volatile elements in the magma chamber, we would expect P_0 to be compressive [*Iverson*, 1995]. However, observations of surface deformation in the rift zone consistently show that it is under horizontal extension, as manifested by the emplacement of vertical dikes [*Lipman et al.*, 1985] and high rate (5-25 cm yr⁻¹) of extension [*Owen et al.*, 1995; *Delaney et al.*, 1998] relative to the characteristic rate of <3 cm yr⁻¹ for intra-

plate deformation [e.g., *Avouact and Tapponnier*, 1993; *England and Molnar*, 1998]. Formation of vertical dikes in the rift zone of the Mauna Loa-Kilauea system is at least permissive for the existence of tensile stress at the surface, which would require that P_0 is negative. An additional uncertainty with assigning P_0 is the introduction of bending stress (tensile at the surface) by magma upwelling. This stress may be superposed on the compressive pressure induced by degassing within the magma chamber. Thus P_0 should be viewed as a composite term contributed by multiple processes. Because of this difficulty we take a try-and-error approach to determine P_0. As shown below, we first search for solutions that satisfy all other boundary conditions discussed above (i.e., wedge top, wedge base, and magmatic density gradient at the back of the wedge) but leave P_0 undetermined. Once a particular solution is found that satisfies the incomplete boundary conditions mentioned above, simulates the observed surface strain and the state of stress in the wedge, and predicts a reasonable magnitude of stress, the solution is used to evaluate P_0.

Equation (36) at $x = X_0$ may be written in terms of normal stress (σ_{xx}) and effective normal stress ($\overline{\sigma}_{xx}$), respectively,

$$\sigma_{xx}(x = X_0) = P_{\text{magma}}, \tag{37}$$

$$\overline{\sigma}_{xx}(x = X_0) = P_{\text{magma}} - P_f = P_{\text{magma}} + \frac{(1-\lambda)\rho_w g y}{\cos\alpha}. \tag{38}$$

By noting that $K_5 = TK_9$, $K_{11} = -3K_9$, and $K_4 = (K_3 Q - S)$, the following relationships that define P_0, K_3, and K_9 may be obtained by comparing (38) with (36) and noting that (38) is also defined in (8) in terms of a general solution derived from the Airy stress function

$$P_0 = -(K_3 X_0 - 6K_9 X_0^2 - X_e X_0), \tag{39}$$

$$K_3 = [\frac{\rho_{\text{magma}}^{z=0} \alpha_0 g \cos\alpha}{12\tan\theta} T - \rho_{\text{magma}}^{z=0} g \cos\alpha$$
$$+ \frac{(1-\lambda)\rho_w g}{\cos\alpha} + S]/Q, \tag{40}$$

$$K_9 = \frac{\rho_{\text{magma}}^{z=0} \alpha_0 g \cos\alpha}{12 X_0 \tan\theta}, \tag{41}$$

where T, Q, and S are defined in (31), (33), and (34). Thus the final solution for the stress distribution within an elastic wedge satisfying the incomplete boundary conditions described above may be written as

$$\overline{\sigma}_{xx} = \frac{1}{Q}[\frac{\rho_{\text{magma}}^{z=0} \alpha_0 g \cos\alpha}{12\tan\theta} T - \rho_{\text{magma}}^{z=0} g \cos\alpha$$
$$+ \frac{(1-\lambda)\rho_w g}{\cos\alpha} + S]x + [\frac{\rho_{\text{magma}}^{z=0} \alpha_0 g \cos\alpha}{12\tan\theta} T$$
$$- \rho_{\text{magma}}^{z=0} g \cos\alpha + \frac{(1-\lambda)\rho_w g}{\cos\alpha}]y$$
$$+ \frac{\rho_{\text{magma}}^{z=0} \alpha_0 g \cos\alpha}{12 X_0 \tan\theta}(xy + 12y^2 - 6x^2)$$
$$+ (1-\lambda)\rho_w g \sin\alpha x, \tag{42}$$

$$\overline{\sigma}_{yy} = -\frac{\rho_{\text{magma}}^{z=0} \alpha_0 g \cos\alpha}{2 X_0 \tan\theta} y^2 - (1-\lambda)\rho_w g \cos\alpha y, \tag{43}$$

$$\sigma_{xy} = -\frac{1}{Q}[\frac{\rho_{\text{magma}}^{z=0} \alpha_0 g \cos\alpha}{12\tan\theta} T - \rho_{\text{magma}}^{z=0} g \cos\alpha$$
$$+ \frac{(1-\lambda)\rho_w g}{\cos\alpha} + S]y$$
$$- \frac{\rho_{\text{magma}}^{z=0} \alpha_0 g \cos\alpha}{12 X_0 \tan\theta}(\frac{1}{2}Ty - 12x)y. \tag{44}$$

Using the similar approach to determining P_0, the shear traction at the back of the wedge may also be evaluated using (44). That is,

$$\sigma_{xy}(x = X_0) = (12K_9 X_0 - K_3)y - \frac{1}{2}TK_9 y^2. \tag{45}$$

This relationship predicts the distribution and magnitude of shear traction along the back of the wedge as required by the solution.

Once the stress distribution is known, we may use Hooke's law to determine the strain distribution in the elastic wedge using the following relationships for a plane strain condition:

$$e_{xx} = \frac{\partial u}{\partial x} = \frac{1}{E}[(1-v^2)(\overline{\sigma}_{xx} - \frac{\lambda\rho g y}{\cos\alpha})$$
$$- v(1+v)(\overline{\sigma}_{yy} - \frac{\lambda\rho g y}{\cos\alpha})], \tag{46}$$

$$e_{yy} = \frac{\partial v}{\partial y} = \frac{1}{E}[(1-v^2)(\overline{\sigma}_{yy} - \frac{\lambda\rho g y}{\cos\alpha})$$
$$- v(1+v)(\overline{\sigma}_{xx} - \frac{\lambda\rho g y}{\cos\alpha})], \tag{47}$$

$$e_{xy} = \frac{1}{2}(\frac{\partial u}{\partial y} + \frac{\partial v}{\partial x}) = \frac{(1+v)}{E}\sigma_{xy}, \tag{48}$$

where e_{xx}, e_{yy}, and e_{xy} are linear and shear strain components, u and v are displacement components in the x and y directions, and E and v are Young's modulus and Poisson's ratio, respectively. The calculated strain components and displacement field may be evaluated at the surface and their values may be compared with geodetically determined strain and displacement distribution.

The boundary condition at the back of the wedge may be simplified by assuming that the vertical density gradient of magma is zero in the rift zone. Under this condition, $\alpha_0 = 0$, equations (39)-(41) become

$$P_0 = (X_e - K_3)X_0, \tag{49}$$

$$K_3 = \frac{1}{Q}[-\rho_{\text{magma}}^{z=0} g \cos\alpha + \frac{(1-\lambda)\rho_w g}{\cos\alpha} + S], \tag{50}$$

$$K_9 = 0. \tag{51}$$

Because $K_6 = K_{10} = 0$ and $K_{11} = -3K_9$, the condition of constant magma density at the back of the wedge effectively drops all the nonlinear terms in (8)-(10). The corresponding solution for stress distribution inside the wedge becomes

$$\overline{\sigma}_{xx} = \frac{-\rho_{\text{magma}}^{z=0} g \cos\alpha + \frac{(1-\lambda)\rho_w g}{\cos\alpha} + S}{Q} x$$
$$- [\rho_{\text{magma}}^{z=0} g \cos\alpha - \frac{(1-\lambda)\rho_w g}{\cos\alpha}]y$$
$$+ (1-\lambda)\rho_w \sin\alpha x, \tag{52}$$

$$\overline{\sigma}_{yy} = -(1-\lambda)\rho_w g y \cos\alpha, \tag{53}$$

$$\sigma_{xy} = \frac{1}{Q}[\rho_{magma}^{t=0}g\cos\alpha - \frac{(1-\lambda)\rho_w g}{\cos\alpha} - S]y. \qquad (54)$$

Note that the effective stress in the y direction ($\bar{\sigma}_{yy}$) is now reduced to a combination of a lithostatic stress and a pore fluid pressure. This relation implies that the wedge is in an isostatic equilibrium when the magma density is constant in the rift zone. The above solutions shown in (52), (53) and (54) are essentially the same as the special solutions obtained by *Yin* [1993] in equations (26), (27), and (28) when we set $K_8 = 0$ in those equations.

3. Results

In order to have a clear physical meaning in comparing our model prediction with the observed stress and strain, our elastic wedge model needs to be qualified. Geodectically determined displacement in the Mauna Loa-Kilauea region is time-dependent [*Delaney et al.*, 1998], which is probably one of the causes for its scattering. As we did not divide the observed strain in terms of their specific time windows being observed (Figure 2), our treatment averages the strain over the entire period of observation that

we interpret to represent an average over a geologic timescale. This assumption is consistent with the assumed boundary conditions. First, our model requires that the entire basal decollement be at the critical state of frictional sliding governed by Amonton's law. However, one may imagine that in the time interval of a few years, only a portion of the basal thrust is at the critical state that leads to earthquake rupture at a small segment of the basal decollement. When we expand the observation to hundreds of thousands of years over several tens of earthquake cycles, the entire decollement may be viewed as in the critical state for frictional sliding. Similarly, we assume in our model a time-independent distribution of magma density at the back side of the rift flank, which prevents us from modeling the effect of transient magmatic intrusion and time-dependent variation of magmatic density caused by differentiation, cooling, and reheating of magma. If our model simulates the long-term effect, then its results may answer questions such as (1) why the measured strain has an upper and lower bound and a characteristic average value and (2) why strain in the Mauna Loa-Kilauea rift flank decreases systematically from the rift zone to the toe of the rift flank. Because our
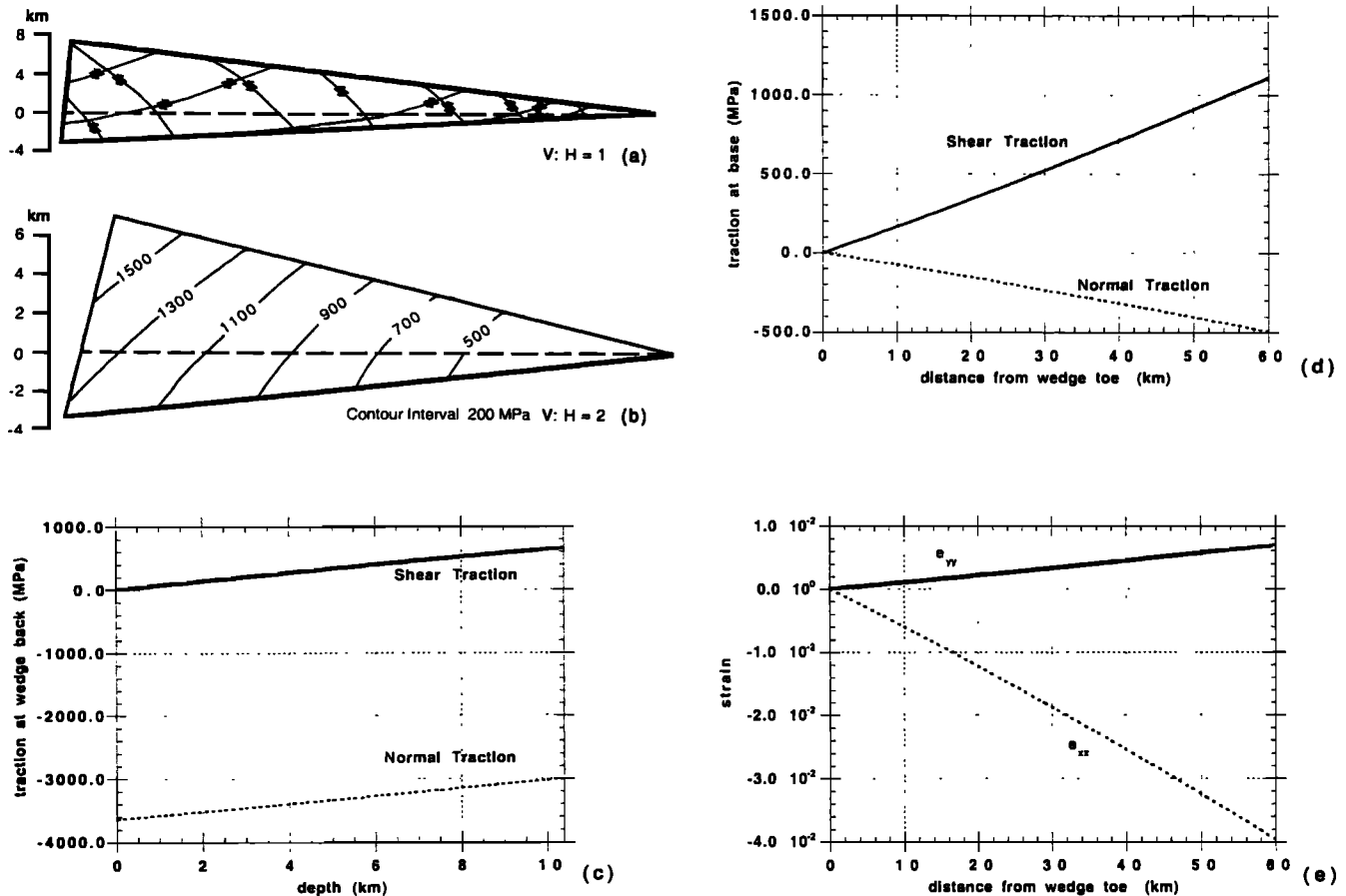

Figure 4. A solution showing (a) predicted fault pattern, (b) distribution of the maximum shear stress, (c) magnitude distribution of normal and shear tractions at the back of the wedge, (d) magnitude distribution of effective normal and shear tractions along the base of the wedge, and (e) magnitude distribution of strain components at the surface. To calculate elastic strain from stress, we assume that Young's modulus E = 89,655 MPa and Poisson's ratio ν = 0.15. The same values are used for all plots shown in Figures 5-9. The following model parameters are used for these results: α_0 = 0.1, α = 7° (surface slope), β = 3° (dip of the basal fault), X_0 = 60 km (length of the wedge), μ_b = 0.7 (basal coefficient of friction), λ = 0.4 (pore fluid pressure ratio for the wedge), λ_b = 0.4 (pore fluid pressure ratio along the basal decollement), ρ_w = 2.7 g cm^{-3} (density of the wedge), and ρ_{magma} (y = 0) = 2.5 g cm^{-3} (density of magma at the surface).
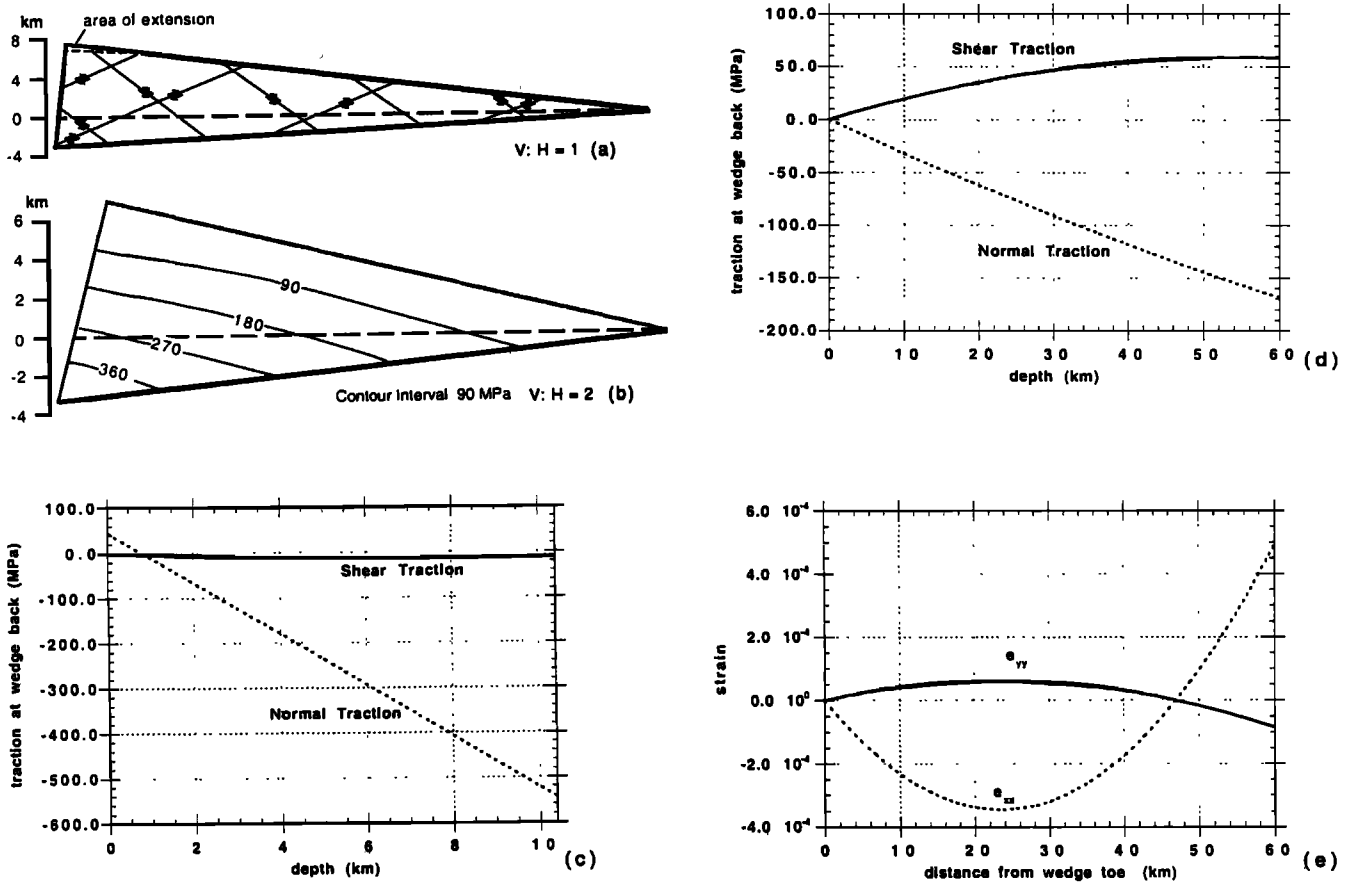
Figure 5. A solution showing (a) predicted fault pattern, (b) distribution of the maximum shear stress, (c) magnitude distribution of normal and shear tractions at the back of the wedge, (d) magnitude distribution of effective normal and shear tractions along the base of the wedge, and (e) magnitude distribution of strain components at the surface. All the parameters are the same as those used in Figure 4 except that $\alpha_0 = -0.05$ and $\lambda = \lambda_b = 0.90$.

model represents the background of stress and strain states, the cause of relatively small temporal variation of the measured strain and stress may be attributed to local and transient perturbations. For example, fluctuation of strain magnitude with time may be attributed to perturbation of stress due to emplacement of magma and dikes, initiation of new faults, and rupturing and sliding along existing fault surfaces. We expect that their effects on the total stress and strain are small. For example, the magnitude of static stress variation triggered by an earthquake of $M = 6.5$ to $M = 7.5$ is typically of the order of 0.1-0.5 MPa [e.g., *King et al.*, 1994].

We calculate the principal stress directions by

$$\psi = \frac{1}{2}\tan^{-1}\left[\frac{2\sigma_{xy}}{\overline{\sigma}_{xx} - \overline{\sigma}_{yy}}\right], \tag{55}$$

where ψ defines the orientation of the greatest principal stress direction with respect to the x axis and the magnitude of the maximum shear stress by

$$\tau_{max} = \sqrt{\frac{1}{4}\left[\overline{\sigma}_{xx} - \overline{\sigma}_{yy}\right]^2 + \sigma^2_{xy}}. \tag{56}$$

We plot potential fault patterns that are inferred from the principal stress directions by using the Coulomb fracture criterion, assuming a 30° angle of internal friction. Although predicted fault patterns are plotted throughout the wedge in all the results (Fig-

ures 4a-9a), it does not mean that brittle failure occurs everywhere. It would be difficult to choose a cutoff value because the estimated shear strength of the lithosphere varies from <1 MPa to several hundreds of megapascals. Here we simply show the distribution of the maximum shear stress for every case and leave the readers to judge their plausibility.

In the following, we show a few examples of the solutions that illustrate both the general properties of the model and the particular solutions that match the observed stress and strain distributions in the Mauna Loa-Kilauea rift system. The case shown in Figure 4 used the following parameters: the vertical gradient of magma density at the back side of the wedge (α_0) is 0.1, the surface slope (α) is 7°, the dip of the basal thrust (β) is 3°, the pore fluid pressure ratio inside the wedge (λ) is 0.4, the pore fluid pressure along the base of the wedge (λ_b) is 0.4, the coefficient of basal friction (μ_b) is 0.7, the magmatic density at the back side of the wedge at the surface (ρ_{magma}) is 2.5 g cm^{-3}, the density of the wedge (ρ_w) is 2.7 g cm^{-3}, and the length of the wedge (X_0) is 60 km. The shape and length of the wedge are constrained by the geometrical dimension of the Mauna Loa-Kilauea rift system shown in Figure 1. Under the above conditions, the entire wedge is occupied by thrust faults (Figure 4a), with the magnitude of the maximum shear stress ranging from ~500 MPa near the toe to >1500 MPa near the back side of the wedge (Figure 4b). The

normal traction at the back of the wedge is entirely compressive, with its magnitude unrealistically high (Figure 4c). The magnitude of the corresponding shear stress at the back also increases with depth, from zero at the surface to about 700 MPa (Figure 4c). The shear and normal tractions at the base of the wedge increase in magnitude from the toe to the back of the wedge (Figure 4d). Finally, the linear strain in the x direction at the surface is contractional, increasing in magnitude from the toe towards the back of the wedge. The corresponding strain component in the y direction is extensional and increases in magnitude from the toe to the back of the wedge (i.e., the rift zone) (Figure 4e). The magnitude of the predicted horizontal strain is two orders of magnitude higher than those observed in the Mauna Loa-Kilauea rift (cf. Figures 2 and 4e).

In Figure 5, we assume that all the parameters are the same as those used in Figure 4 except $\alpha_0 = -0.05$ and $\lambda = \lambda_b = 0.90$. Under these conditions, tensile stress is predicted in the upper left corner of the rift flank at the back, and the rest of the wedge is in compression (Figure 5a). The magnitude of the maximum shear stress inside the wedge varies from <90 MPa near the top of the wedge to >360 MPa in the lower left corner near the back of the wedge (Figure 5b). Tensile stress of about 50 MPa (i.e., P_0) is predicted in the very top part of the rift back (~1 km thick) (Figure 5c). This value is about a factor of 2 to 3 higher than the highest tensile strength of rock measured in the laboratory (i.e.,

~15-20 MPa [see *Jeager and Cook*, 1979]). The magnitude of both the shear and normal tractions at the base increases from the toe to the back (Figure 5d). The predicted linear strain in the x direction at the surface is on the same order of magnitude (10^{-4}) as those measured (see Figures 2 and 5d). It is extensional near the back of the rift and becomes contractional towards the toe. The crossing point between extension and contraction is at ~47 km from the toe. In Figure 2, we also show the predicted horizontal strain for $\mu_b = 0.60$ and $\mu_b = 0.75$, respectively with all other parameters the same as those for Figure 5. The comparison between observation and prediction shown in Figure 2 suggests that the coefficient of basal friction is in the range of 0.6-0.75 with $\lambda_b = 0.90$ along the basal decollement of the Kilauea-Mauna Loa rift system. The predicted strain component at the surface in the y direction is contractional near the back of the wedge but extensional towards the toe (Figure 5e). The predicted contractional strain near the rift zone is consistent with the geodetic observation that the Kilauea summit has subsided continuously in the past two decades [*Delaney et al.*, 1998]. The predicted strain components in the x and y directions cannot be compared exactly with the observed horizontal and vertical linear strain at the surface because they are at an angle equal to the surface slope. But the difference of the strain values before and after the correction of the surface slope is <0.7% for $\alpha = 7°$, negligible compared to the large spread of the observed strain data. Thus, in the above
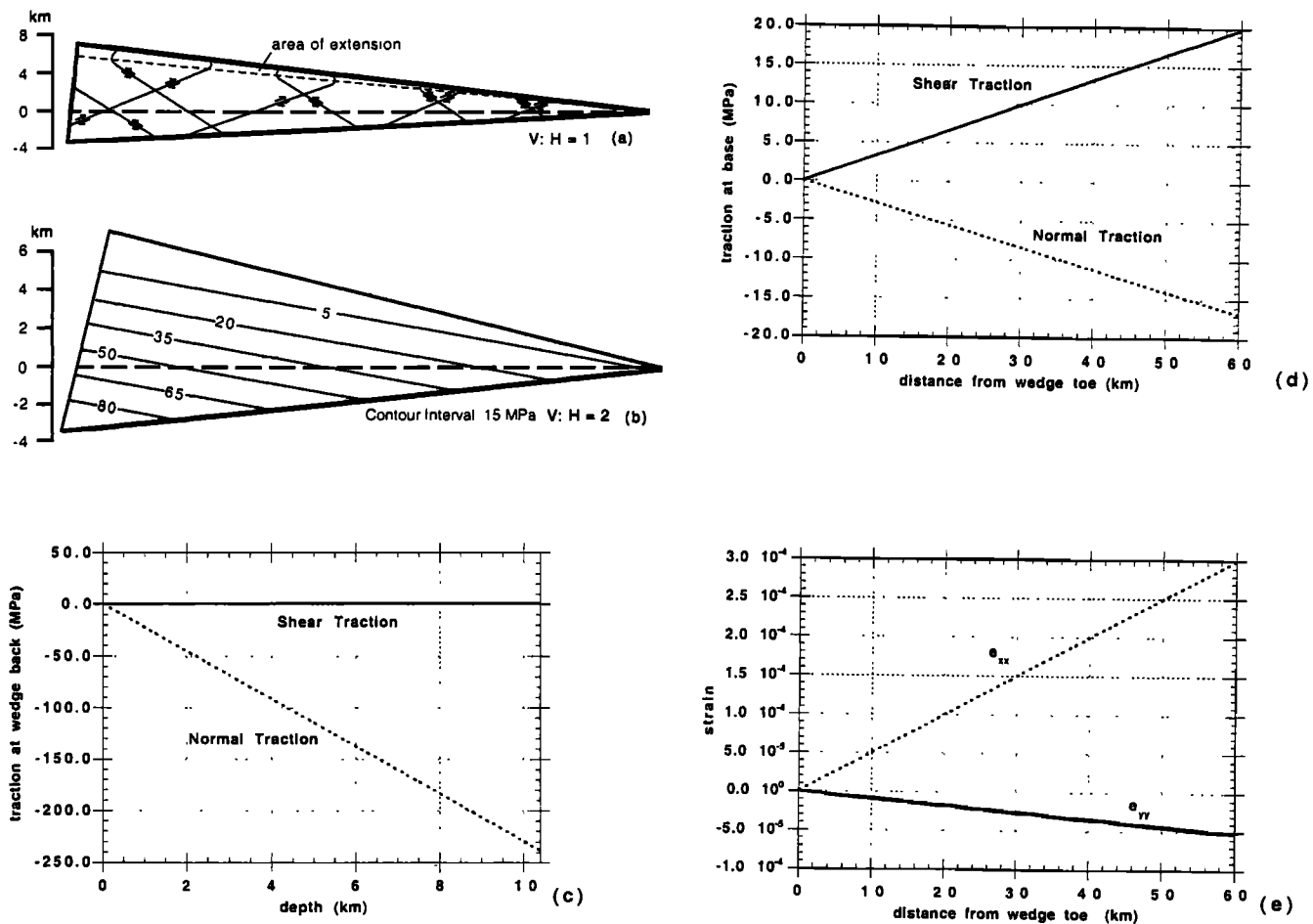

Figure 6. A solution showing (a) predicted fault pattern, (b) distribution of the maximum shear stress, (c) magnitude distribution of normal and shear tractions at the back of the wedge, (d) magnitude distribution of effective normal and shear tractions along the base of the wedge, and (e) magnitude distribution of strain components at the surface. All the parameters are the same as those used in Figure 5 except that $\alpha_0 = 0.0$, $\lambda = \lambda_b = 0.95$, and $\mu_b = 0.25$.
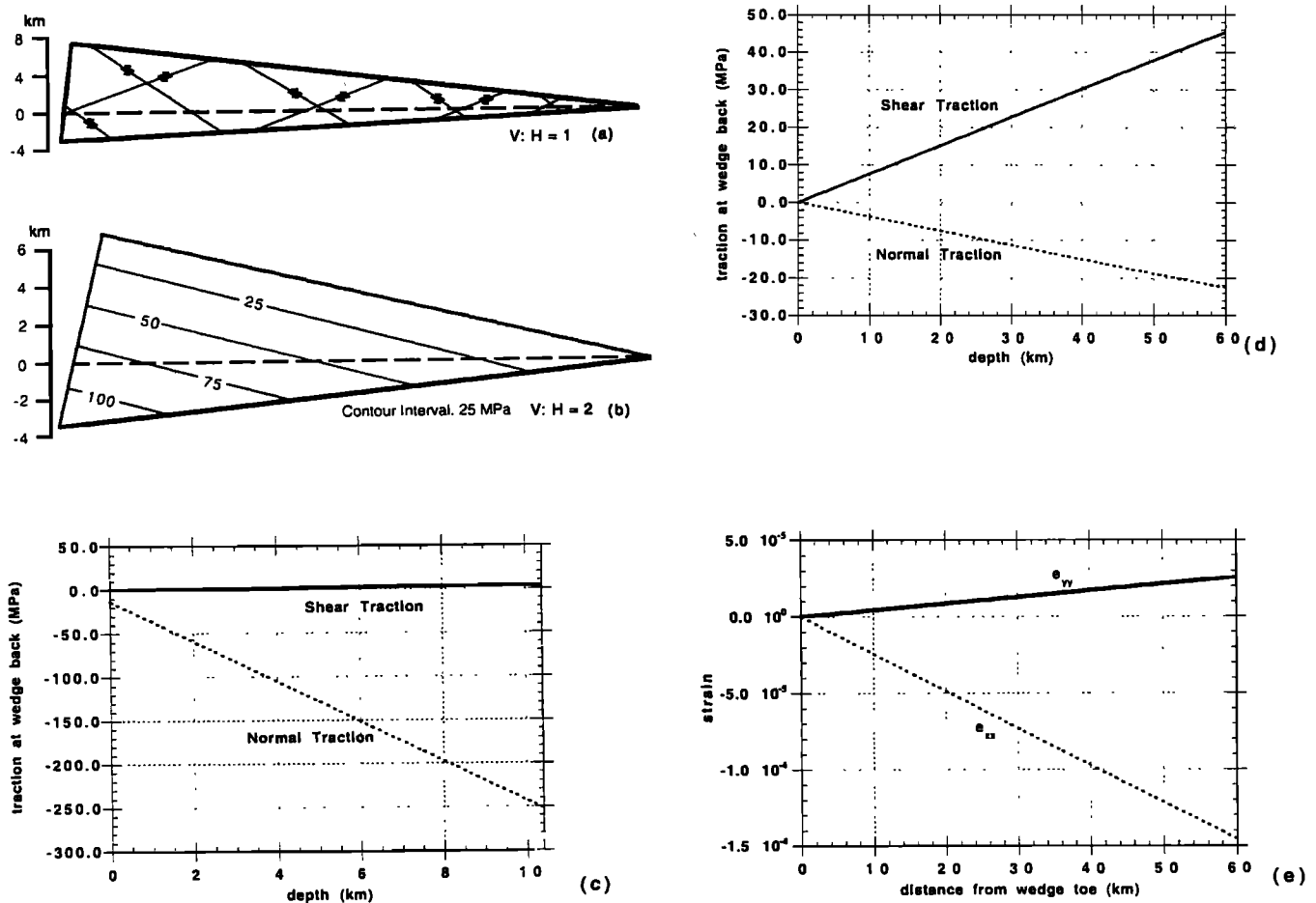
Figure 7. A solution showing (a) predicted fault pattern, (b) distribution of the maximum shear stress, (c) magnitude distribution of normal and shear tractions at the back of the wedge, (d) magnitude distribution of effective normal and shear tractions along the base of the wedge, and (e) magnitude distribution of strain components at the surface. All the parameters are the same as those used for Figure 6 except that $\mu_b = 0.40$.

and the following discussion, we compare the predicted and observed strains directly.

In Figure 6, we assume that $\alpha_0 = 0.0$, $\mu_b = 0.25$, and $\lambda = \lambda_b = 0.95$, with all other parameters held the same as those used for the solution shown in Figure 5. This solution predicts normal faulting in the top part of the wedge and thrusting in the lower part of the wedge (Figure 6a). The maximum shear stress inside the wedge varies from <5 MPa at the surface to >80 MPa in the lower left corner near the back of the wedge (Figure 6b). The predicted maximum tensile stress at the back of the wedge (i.e., P_0) in this case is ~27 MPa (Figure 6c). The magnitude of the shear traction on the back of the wedge increases linearly from zero at the surface to ~2 MPa at the base of the wedge (Figure 6c). Shear and normal tractions at the base increase in magnitude from the toe to the back of the wedge (Figure 6d). The predicted magnitude of strain in the x direction and the trend of its variation match well the observed horizontal strain (see Figures 2 and 6e). In addition, the predicted strain component in the y direction is contractional, increasing in magnitude from the toe to the back of the wedge (Figure 6e). Similar to the case shown in Figure 5, we also plot two other predicted horizontal strain distributions with the coefficient of basal friction $\mu_b = 0.10$ and $\mu_b = 0.35$ in Figure 2. When $\mu_b = 0.35$, the maximum tensile traction predicted at the

back of the wedge is only ~6 MPa, and the predicted fault pattern is similar to that shown in Figure 6a. If the entire upper part of the Kilauea-Mauna Loa rift flank experiences extension, then the results shown in Figures 6e and 2 indicate that its basal decollement has a coefficient of friction of 0.10-0.35.

The key difference between the predicted strain patterns in Figures 5e and 6e is whether the frontal portion of the rift flank is under contraction or extension. A recent seismic reflection study appears to favor the prediction shown in Figure 5e (i.e., contraction occurs in the frontal part of the wedge while extension near the rift zone) [Morgan et al., 2000]. However, it is not clear whether the structures imaged by the seismic-reflection study are active or not. Thus a definitive answer requires geodetic survey of the submerged portion of the rift flank in the future.

From the results shown in Figure 2, it is clear that solutions shown in both Figures 5 and 6 are very sensitive to the assumed coefficient of basal friction. This can also be demonstrated in Figure 7, which assumes that all the conditions are kept the same as those used for Figure 6 except that μ_b is increased from 0.25 to 0.4 and shows that the wedge becomes completely compressional (Figure 7a). This solution requires that P_0 at the back of the wedge is compressive with its magnitude to be ~12 MPa.

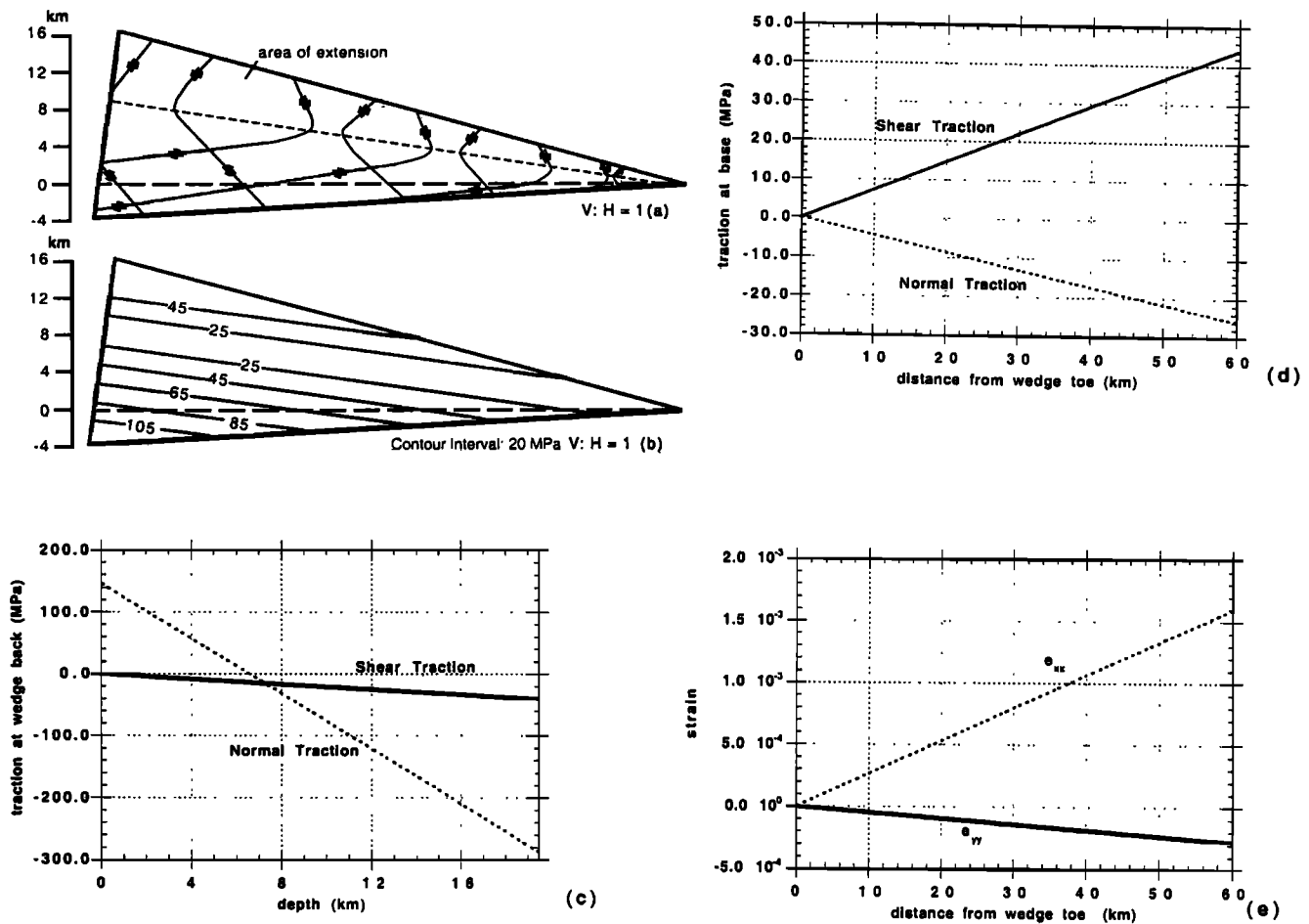Our solutions are also sensitive to the geometry of the wedge.

Figure 8. A solution showing (a) predicted fault pattern, (b) distribution of the maximum shear stress, (c) magnitude distribution of normal and shear tractions at the back of the wedge, (d) magnitude distribution of effective normal and shear tractions along the base of the wedge, and (e) magnitude distribution of strain components at the surface. All the parameters are the same as those used in Figure 7 except that the surface slope increases from 7° to 15°.

For example, when the surface slope of the wedge in Figure 7 increases from 7° to 15°, it leads to extension in the shallow part of the thrust wedge (Figure 8). However, it is also important to note that the presence of a surface slope is not a necessary condition for the occurrence of extension inside the wedge. Extension may occur even though the surface slope is assigned to be zero (Figure 9). The high sensitivity of the solutions to the model parameters suggests that the state of stress and its distribution in the Mauna Loa-Kilauea rift system may have varied temporally in its long geologic history during which both the surface slope and the basal coefficient of friction may have changed with time.

4. Discussion

4.1. Limitations of the Model

Several assumptions are made in our model. For example, we assume that the Mauna Loa-Kilauea rift system behaves as a homogenous and isotropic elastic solid. However, the presence of layered basalts and intrusive bodies of varying geometries in the rift system implies that these assumptions are oversimplistic. However, the most critical assumption of the model is that the normal and shear tractions at the back of the wedge are distributed as a function of a second order polynomial of y, as shown in

(36) and (45). This functional form of traction distribution is in turn dictated by the form of the Airy stress function assumed as in (5). Because the boundary conditions used for obtaining the solutions are incomplete, there are inevitably many Airy stress functions that may also satisfy the incomplete boundary conditions described above (i.e., the wedge top and base). However, the nonuniqueness of the problem does not preclude obtaining viable solutions such as the approach we take here. That is, after assuming their functional form, the exact magnitude and distribution of the tractions at the back side of the wedge can be specified by a trial-and-error approach of matching the solutions with the observed stress and strain distributions, such as the cases shown in Figures 5 and 6. This means that the solutions are self-consistent. Nevertheless, our study represents the first attempt that uses a dynamic model to simultaneously explore the traction conditions needed to explain the state of stress and the observed strain in the Mauna Loa-Kilauea rift system. This is in contrast to many early studies that address how deformation has occurred by not knowing why it has occurred in the rift system [i.e., *Wallace and Delaney*, 1995; *Owens et al*, 1995].

The inferred high pore fluid pressure above the hydrostatic pressure from our solutions (Figure 2) within the wedge implies that the fluid flow in the rift flank may not be in a steady state.
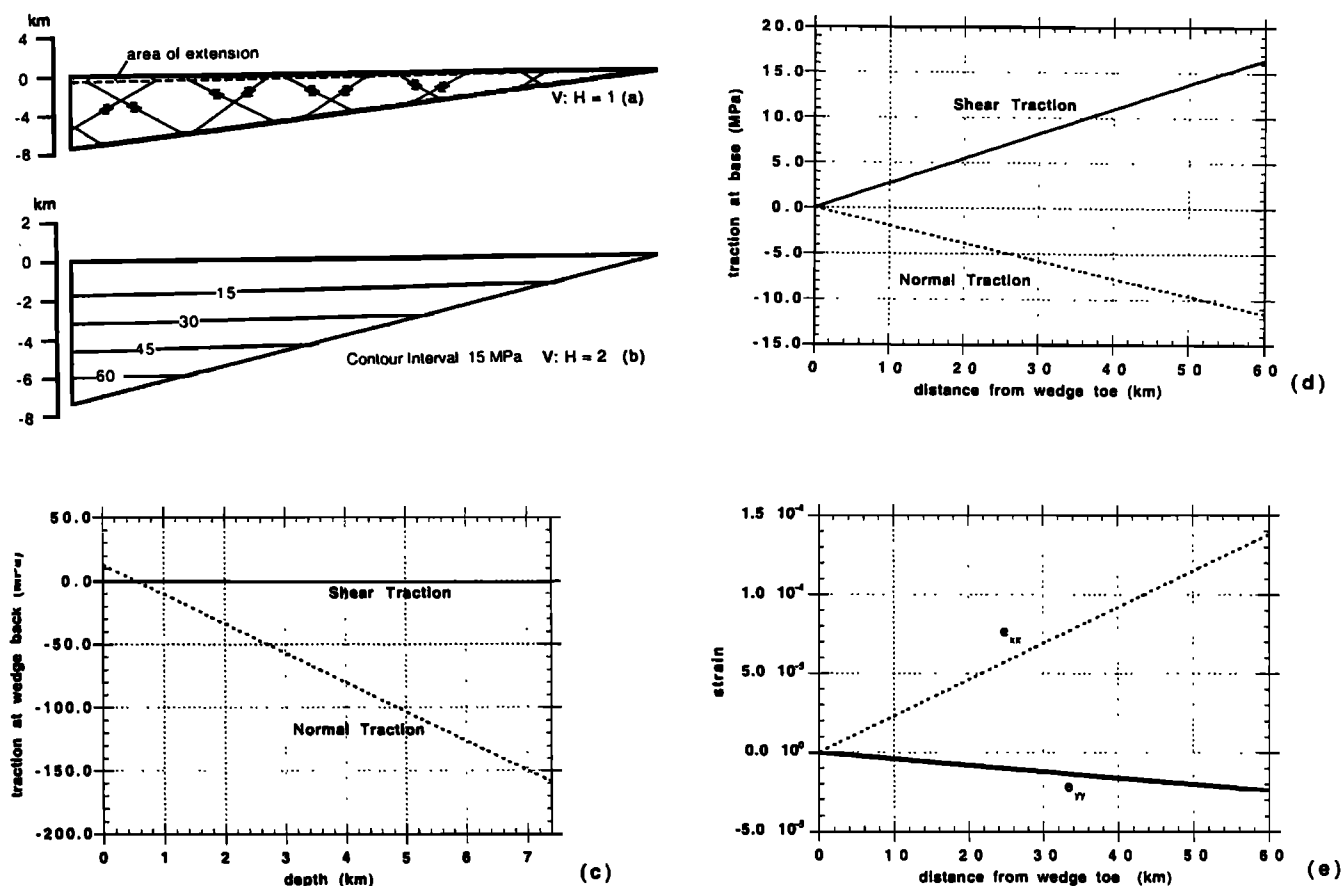
Figure 9. A solution showing (a) predicted fault pattern, (b) distribution of the maximum shear stress, (c) magnitude distribution of normal and shear tractions at the back of the wedge, (d) magnitude distribution of effective normal and shear tractions along the base of the wedge, and (e) magnitude distribution of strain components at the surface. The following parameters are used: $\alpha_0 = 0.0$, $\alpha = 0°$ (surface slope), $\beta = 7°$ (dip of the basal fault), $X_0 = 60$ km (length of the wedge), $\lambda = \lambda_b = 0.95$ (pore fluid pressure ratio at the base), $\mu_b = 0.1$ (coefficient of basal friction), $\rho_w = 2.7$ g cm^{-3} (density of wedge), and ρ_{magma} ($y = 0$) = 2.5 g cm^{-3} (density of magma at the surface).

Rigorously speaking, determining stress distribution in the rift flank is a coupled problem. That is, the evolution of pore fluid pressure should be solved simultaneously with the solution of stress distribution [e.g., *Walder and Nur*, 1984]. However, as the source term of fluid flux, permeability distribution, and boundary conditions of fluid flow or fluid pressure are all poorly constrained, taking such a sophisticated approach at this stage may obscure the first-order mechanics of the rift system.

Despite the limitation of nonuniqueness and a few unrealistic assumptions, the solutions derived from this approach do make specific predictions that can be tested further in the future. For example, the existence of tensile stress and its systematic variation with depth may be tested by deep drilling. Whether the magmatic density and the tensile stress gradient represented by parameter α_0 are constant or vary with depth in the rift zone can also be tested by obtaining more coverage of strain measurements at the surface in the submerged part of the rift flank. This would be the key to differentiating two solutions shown in Figure 2, both fitting the observed strain data well. Finally, the solutions presented here also highlight the need for measuring vertical strain and strain distribution in the vertical direction (i.e., the vertical gradient of the strain components).

4.2. Implications of the Model Predictions

Consideration of (1) a reasonable magnitude of the tensile traction predicted at the back side of the wedge ($<$~20-30 MPa), (2) a reasonable range of magnitude of the maximum shear stress within the wedge ($<$100 MPa), (3) an overall match of the observed stress distribution (i.e., coeval extension in the top and contraction in the bottom of the wedge), and (4) the strain variation at the surface from the Mauna Loa-Kilauea rift system led us to conclude that the solutions shown in Figure 6 provides the best simulation. Such a solution has several important implications. First, it implies that normal faults observed on the surface are only restricted in the very shallow part of the rift system. Second, a tensile stress of the order of ~6-30 MPa must have existed in the rift zone near the surface. Third, not only the effective coefficient of basal friction is required to be low (i.e., $\mu_b = 0.25$-0.35, and $\lambda_b = 0.95$), but the pore fluid pressure within the wedge must also have been elevated to be significantly above the hydrostatic state (i.e., $\lambda = 0.95$).

The required low effective coefficient of basal friction may be induced by several processes operated along the base of the Mauna Loa-Kilauea rift flank. First, fluids derived from upwell-

ing of the magma may be injected into both the rift flank within the wedge and along the interface between the volcanic pile of the rift flank and the underlying oceanic floor. This process would have increased the pore fluid pressure within and along the base of the wedge. Second, compaction of preexisting, water-saturated oceanic sediments by continuous loading of volcanic pile through successive eruptions could have generated and maintained a high pore fluid pressure along the basal decollement. Another possible mechanism for generating abnormal pore fluid pressure along the basal decollement is the fault valve behavior of *Sibson* [1992], which has been successfully demonstrated by numerous field examples [e.g., *Cox*, 1995]. This hypothesis postulates that cyclic fluctuation in shear stress and fluid pressure may occur in active fault zones. The variation of fluid pressure may be related to episodic rupture along faults that produces cyclic exchange of fluids between fault zones and their host rocks. This in turn could lead to generation of transient lithostatic fluid pressure in fault zones (i.e., $\mu_b \approx 1.0$) [*Sibson*, 1992; *Cox*, 1995].

The coefficient of friction along the basal decollement of the Kilauea-Mauna Loa rift flank may be significantly reduced from the typical values of 0.7-1.1 as determined by the Byerlee law [1978], owing to the presence of clay minerals in the marine sediments along the interface between the volcanic pile of the rift flank and the underlying oceanic floor [*Ando*, 1979; *Nakamura*, 1980; *Hill and Zucca*, 1987; *Wyss*, 1988]. They are expected to yield a low coefficient of friction of the order of 0.1 as shown by the results of experimental rock mechanics [e.g., *Byerlee*, 1978]. This inference is consistent with the result obtained in Figure 6e.

The predicted tensile stress at the back of the wedge is at first counterintuitive, as it is exactly opposite to what we envisioned at the start of the analysis (i.e., the excess pressure in the magma chamber should be compressive due to devolatilization [see *Iverson*, 1995]). However, such prediction is consistent with the observed emplacement of vertical dikes and fast rates of horizontal extension in the rift zone [*Lipman et al.*, 1985; *Owen et al.*, 1995; *Delaney et al.*, 1998]. The key issue is what has induced the tensile stress. As shown in Figure 8, a large surface slope may in-

duce extension inside the elastic wedge. However, neither the presence nor absence of a topographic slope is required to generate normal faults within the wedge according to our model (Figures 6 and 9). Thus other mechanisms may have been responsible for creating the predicted tensile stress in the rift zone (i.e., Figures 5 and 6). One of the possible causes is upward bending of the overall Mauna Loa-Kilauea rift system. The likelihood of this mechanism may become apparent if we compare the distribution of normal traction along the back of the wedge with that induced by bending of an elastic plate (Figure 10; cf. Figure 6c); both have tensile stress in the upper part, compressive stress in the lower part, and a neutral point (zero normal traction) in between that separates the two regions.

The inferred upward bending may be caused by one or a combination of the following processes (Figure 11a): (1) upward push by buoyant magma along a narrowing-upward magma conduit, (2) emplacement of magma at the base of the volcanic pile that causes doming of the overall rift system, and (3) a bending moment produced by the buoyancy effect of the magma chamber.

Two possible interactions may have occurred between the excess compressive pressure deviating from its lithostatic pressure and the tensile stress generated by bending of the rift system. First, the compressive pressure in the upper part of the rift zone would be reduced by the presence of a tensile stress. That is, the excess pressure P_0 in (36) and (39) should be viewed as a summation of two terms: $P_0 = P_{ex} - P_b$, where P_{ex} is the excess magmatic pressure of *Iverson* [1995] deviating from the lithostatic pressure, and P_b is the tensile stress induced by bending. In particular, P_0 is tensile when $P_b > P_{ex}$. Since these two terms determine the magnitude of P_0 which in turn decides the location of the neutral point on the back of the wedge, the exact distribution of traction on the wedge back may differ from that for a pure bending situation. In the latter case, the neutral point is always located at the midpoint of the section (Figure 10b).

An alternative explanation for the generation of the predicted tensile stress in the upper part and compressive stress in the lower part of the rift zone is that the emplacement of magma along the
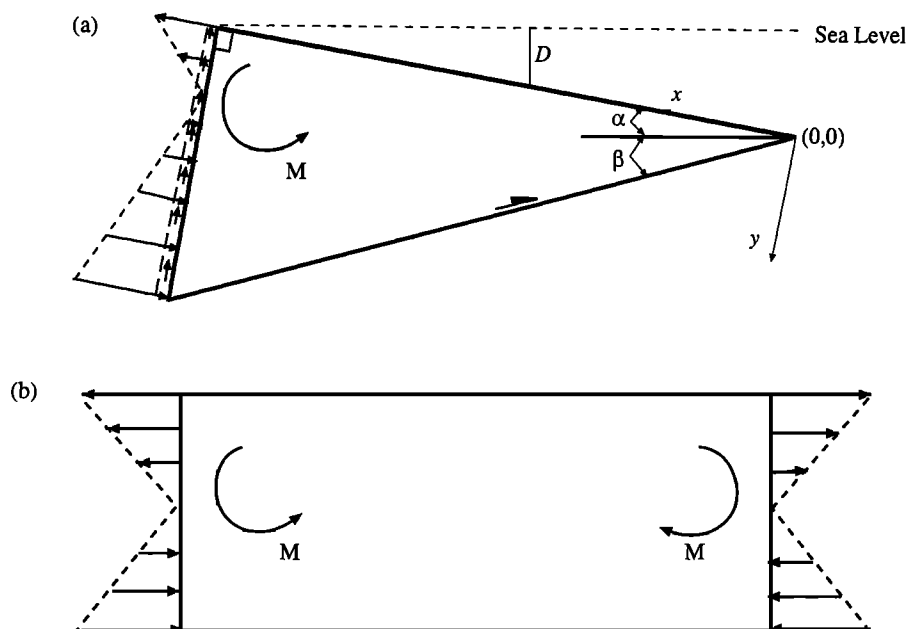

Figure 10. A qualitative comparison of stress distribution along (a) the back of the wedge required by elastic solutions shown in Figures 5 and 6 and (b) stress distribution in an elastic plate under pure bending condition.
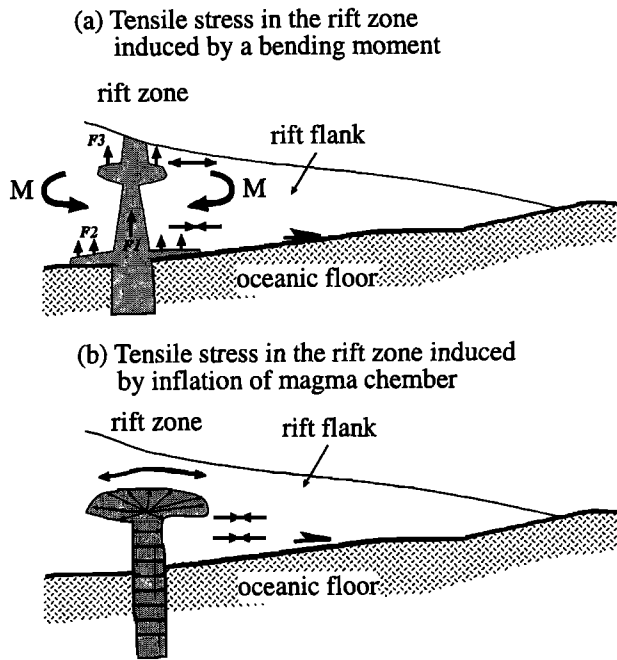
(a) Tensile stress in the rift zone induced by a bending moment

rift zone

(b) Tensile stress in the rift zone induced by inflation of magma chember

Figure 11. Possible mechanisms for creating tensile stress in the upper part of the rift zone as required by the stress solutions shown in Figures 5 and 6. (a) Bending of the rift flank induced by one or a combination of the following processes: (1) upward push by buoyant magma along a narrowing-upward magma conduit (F1), (2) emplacement of magma at the base the volcanic pile that causes doming of the rift zone (F2), and (3) a bending moment produced by the buoyancy effect of the magma chamber (F3). (b) Tensile stress at the back of the wedge possibly produced by inflation of magma chamber at a shallow crustal level. Expansion of magma in the conduits produces horizontal push causing compression in the lower part of the wedge.

magma conduit provides horizontal compression in the rift flank when it spreads laterally (Figure 11b), as proposed by *Borgia* [1994]. The magma chamber above the conduit at a shallow crustal level inflates [e.g., *Yang et al.*, 1992], which would have produced a tensile stress in the upper part of the rift zone. This is similar to the model proposed by *Nettles and Ekstrom* [1998] for explaining earthquake mechanisms near Bardarbunga Volcano, Iceland.

4.3. Vertical Displacement and Vertical Strain

The predicted strain in the y direction by our preferred solutions (Figures 5 and 6) can not be directly compared with the magnitude of subsidence and uplift at the surface because we do not know the vertical gradient of the vertical displacement through which we can calculate the vertical linear strain. However, some qualitative comparisons could be made. First, the predicted strain near the rift zone in the y direction is contractional (i.e., vertical thinning) with its maximum value centered at the back of the wedge. This matches well the observed maximum subsidence in the rift zone (Figures 5e and 6e). Second, the predicted strain in the y direction for the frontal part of the rift flank is contractional (i.e., vertical thickening, see Figure 5e), which may explain why the rift flank is uplifted. Although the predicted and the observed vertical displacement patterns are qualitatively consistent, the measured vertical displacement at the surface with respect to the sea level may be contributed by at least three proc-

esses: (1) internal deformation of the rift flank as simulated by this study, (2) thermal subsidence induced by cooling of the magma chambers or uplift caused by inflation of the magma chamber, and (3) the upslope translation of the wedge-shaped block along the basal decollement. The last two processes cause an upward translation of the reference framework used by this study (see Figures 2 and 3). Unless the last two sources of vertical motion for the rift system can be removed and the vertical gradient of the vertical displacement (i.e., the vertical strain) can be measured, it is at present difficult to compare our vertical strain results directly against the observed subsidence and uplift pattern in the Kilauea region.

4.4. Fault Patterns in Cross Section

Although the predicted fault patterns in this study (e.g., Figure 6a) may grossly resemble that shown in Figure 1b, there is a prominent difference between the two models. The normal faults predicted by this solution do not represent breakaway zones of a series of landslides in the upper part of the rift flank as envisioned by *Gillard et al.* [1996], which requires the presence of several thrust toes on the top of rift flank. Instead, we suggest that the normal faults flatten downward and merge with a zone of low-angle faults. Similarly, thrust faults in the deeper part of the wedge merge upward with a zone of low-angle faults and are linked downward with the basal decollement to form a thrust duplex characteristic to fold-thrust belts [e.g., *Yin and Kelty*, 1991]. A possible fault pattern on cross section based on solution shown in Figure 6a is depicted in Figure 12.

4.5. Lava Fountains in Puu Oo

The Lava pond in Puu Oo (Figure 1) had maintained a static level of 20-200 m above the ground surface during which the surface displacement data were used to match our model prediction. This observation appears to contradict our model result that P_0 is negative, requiring the rift zone at the surface in tension. As we mentioned above, P_0 should be viewed as a composite term that represents the sum of excess magmatic pressure and the regional stress that superimposed on. Thus only looking at its net value cannot constrain the excess magma pressure. Leaving this interpretation aside, there are at least two other ways to explain this observation. First, the high excess magmatic pressure as expressed by eruption of magma in Puu Oo is related to degassing of the volatile in the very top part of the magma chamber. This means that the excess pressure is both short-lived in time and localized in space (that is, only the very top part of the magma
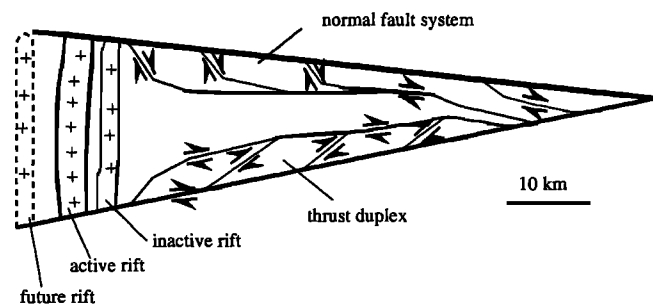

Figure 12. Possible fault pattern on cross-sectional view in the Mauna Loa-Kilauea rift system. The normal faults in the upper part of the wedge and thrust faults in the lower part of the wedge merge with a zone of low-angle faults in the central portion of the wedge. The thrust faults in the lower part may form a duplex structure with the decollement as its sole thrust.

chamber and the wedge back are affected by this boundary condition). However, the excess pressure as defined by P_0 in our model is applied for the entire back of the wedge over the length of the rift zone. When considering that our model deals with the long-term average state of stress in the rift flank, the transient process of magma eruption may be regarded as a small perturbation to the background stress state modeled by our elastic solutions. Second, the explanation for the excess magmatic pressure in Puu Oo might be even simpler. Puu Oo is located at a relatively low elevation (~700 m above the sea level) in the rift zone that connects with the Kilauea volcanic summit (~1300 m) and Mauna Loa summit (>3000 m). Such a difference in magma head is sufficient to allow molten magma to migrate via underground fractures along the rift zone from high regions to low regions. It would not be surprising if the magma fountain goes even higher if this driving mechanism indeed operates, as the pressure head between Kilauea and Puu Oo is more than 500 m.

5. Conclusions

1. Two conditions are required to simulate the observed stress and strain distributions in the Mauna Loa-Kilauea rift system: (1) the pore fluid pressure ratio within the wedge (λ) and along the basal decollement (λ_b) must be exceedingly high (i.e., $\lambda = \lambda_b = 0.90$-$0.95$), and (2) a tensile stress on the order of 6-27 MPa must have existed in the very top part of the rift zone at the back of the wedge-shaped rift flank.

2. We attribute the required tensile stress in the rift zone to either upward bending of the Hawaiian volcanic pile induced by emplacement of magma, or inflation of a shallow magma chamber beneath the calderas. In any case, this would suggest that the magma emplacement in the shallow part of the rift zone is a passive process, although the deeper part of the rift zone may have experienced forceful emplacement (i.e., active rifting), producing contraction in the lower part of the rift flank.

3. The solutions obtained by the elastic wedge model are highly sensitive to the wedge geometry and the coefficient of basal friction, implying that the state of stress and its distribution in the Mauna Loa-Kilauea rift system may have varied temporally during the developmental history of the rift system, as both the surface slope and the basal coefficient of friction may have changed at various timescales.

4. Our model suggests that to obtain the strain pattern observed on the surface of the rift flank and the vertical variation of faulting style within the rift flank, the upper part of the rift must hold back the upper part of the rift flank while the lower part of the rift pushes away the lower part of the rift flank. Thus the problem of understanding the coexisting normal faults on the surface of the rift flank and thrust faults deep inside the rift flank is shifted to the problem of understanding the vertical stress distribution along the rift zone.

References

Ando, M., The Hawaii earthquake of November 29, 1975: Low dip angle faulting due to forceful injection of magma, *J Geophys. Res.*, *84*, 7616-7626, 1979.

Avouac, J.P., and P. Tapponnier, Kinematic model of active deformation in central Asia, *Geophys. Res. Lett.*, *20*, 895-898, 1993

Borgia, A., Dynamic basis of volcanic spreading, *J. Geophys. Res.*, *99*, 17,791-17,804, 1994.

Borgia, A., and B. Treves, Volcanic plates overriding the ocean crust: Structure and dynamics of Hawaii volcanoes, in *Ophiolites and Their Modern Oceanic Analogues*, edited by L. M Parson, J. B. Murton, and P. Browning, *Geol. Soc. Spec. Publ.*, *60*, 277-299, 1992.

Byerlee, J , Friction of rocks, *Pure Appl. Geophys.*, *116*, 615-626, 1978.

Clague, D. A., and G. B. Dalrymple, The Hawaiian-Emperor volcanic chain. part 1, Geologic evolution, in *Volcanism in Hawaii*, edited by R. W. Decker, T. L. Wright, and P. H. Stauffer, *U.S. Geol. Surv. Prof. Pap.*, *1350*, 5-54, 1987.

Clague, D. A., and R. P. Denlinger, The role of dunite cumulate in destabilizing the flanks of Hawaiian volcanoes, *Bull. Volcanol.*, *56*, 425-434, 1994.

Cox, S. F., Faulting processes at high fluid pressures: An example of fault valve behavior from the Wattle Gully Fault, Victoria, Australia, *J. Geophys. Res.*, *100*, 12,841-12,859, 1995.

Dahlen, F. A., Noncohesive critical Coulomb wedges: An exact solution, *J. Geophys. Res.*, *89*, 10,125-10,133, 1984.

Davis, D., J. Suppe, and F. A. Dahlen, Mechanics of fold-and-thrust belts and accretionary wedges, *J. Geophys Res.*, *88*, 1153-1172, 1983.

Davis, P. M., Surface deformation due to inflation of an arbitrarily oriented triaxial ellipsoidal cavity in an elastic half space, with reference to Kilauea Volcano, Hawaii, *J. Geophys. Res.*, *91*, 7429-7438, 1986.

Decker, R. W., T. L., Wright, and P. H. Staufer (Eds.), Volcanism in Hawaii, *U S. Geol. Surv. Prof. Pap. 1350*, 1667 pp., 1987.

Delaney, P. T., R. S. Fiske, A. Miklius, A. T. Okamura, and M. K. Sato, Deep magma body beneath the summit and rift zones of Kilauea Volcano, Hawaii, *Science*, *247*, 1311-1316, 1990.

Delaney, P. T, A. Miklius, T. Arnadottir, A. T. Okamura, and M. K. Sako, Motion of Kilauea Volcano during sustained eruption from the Puu Oo and Kupaianaha vents, 1983-1991, *J Geophys. Res.*, *98*, 17,801-17,820, 1993.

Delaney, P, R P. Denlinger, M. Lisowski, A. Miklius, P. G. Okubo, A. T. Okamura, and M. K. Sako, Volcanic spreading at Kilauea, 1976-1996, *J. Geophys. Res.*, *103*, 18,003-18,023, 1998.

Denlinger, R. P., and P Okubo, Structure of the mobile south flank of Kilauea Volcano, Hawaii, *J. Geophys. Res.*, *100*, 24,499-24,507, 1995.

DePaolo, D. J., and E. M. Stolper, Models of Hawaiian volcano growth and plume structure: Implications of results from the Hawaii Scientific Drilling Project, *J. Geophys. Res.*, *101*, 11,643-11,654, 1996.

Dieterich, J. H., Growth and persistence of Hawaiian volcanic rift zones, *J. Geophys. Res.*, *93*, 4258-4270, 1988.

England, P., and P. Molnar, The field of crustal velocity in Asia calculated from Quaternary rates of slip on faults, *Geophys. J. Int.*, *130*, 551-582, 1998.

Fiske, R. S , and E D. Jackson, Orientation and growth of Hawaiian volcanic rifts: The effect of regional structure and gravitational stresses, *Proc. R. Soc. London, Ser. A, 329*, 43, 299-326, 1972.

Fung, Y. C., *Foundation of Solid Mechanics*, 593 pp., Chapman and Hall, New York, 1965.

Gillard, D., M. Wyss, and P. Okubo, Type of faulting and orientation of stress and strain as a function of space and time in the Kilauea's south flank, Hawaii, *J. Geophys Res.*, *101*, 16,025-16,042, 1996

Hill, D. P., and J. J. Zucca, Geophysical constraints on the structure of Kilauea and Mauna Loa volcanoes and some implications for seismomagmatic processes, in *Volcanism in Hawaii*, edited by R. W. Decker, T. L Wright, and P. H. Stauffer, vol. 2, *U.S. Geol. Prof Pap.*, *1350*, 903-917, 1987.

Hubbert, M. K., and W W. Rubey, The role of fluid pressure in mechanics of overthrust faulting, I, Mechanics of fluid-filled porous solids and its application to overthrust faulting, *Geol. Soc. Am Bull.*, *70*, 115-166, 1959.

Iverson, R. M., Can magma-injection and groundwater forces cause massive landslide on Hawaiian volcanoes?, *J. Volcano. Geotherm. Res.*, *66*, 295-308, 1995.

Jaeger, J. C., and N G. W. Cook, *Fundamental of Rock Mechanics*, 593 pp., Chapman and Hall, New York, 1979.

King, G.C.P, R.S. Stein, and J. Lin, Static stress changes and the triggering of earthquakes, *Bull. Seismol. Soc. Am.*, 84, 935-953, 1994.

Lipman, P. W., The southwest rift zone of Mauna Loa: Implications for structural evolution of Hawaiian Volcanoes, *Am. J. Sci.*, 280-A, 752-776, 1980.

Lipman, P. W., J. P. Lockwood, R. T Okamura, D. A. Swanson, and K. M. Yamashita, Ground deformation associated with the 1975 magnitude-7.2 earthquake and resulting changes in activity of Kilauea volcano 1975-1977, Hawaii, *U.S. Geol. Surv. Prof. Pap.*, 1276, 45 pp., 1985.

Melosh, H. J., and A. Raefsky, The dynamic origin of subduction zone topography, *Geophys. J. R. Astron. Soc.*, 60, 333-354, 1980.

Melosh, H J, and C. A. Williams Jr., Mechanics of graben formation in crustal rocks· A finite element analysis, *J Geophys. Res.*, 94, 13,961-13,973, 1989.

Moore, J G., and H. L. Krivoy, The 1962 flank eruption of Kilauea Volcano and structure of the east rift zone, *J. Geophys. Res.*, 69, 2033-2045, 1964.

Moore, J. G., W. B. Bryan, M H. Beeson, and W. R. Normark, Giant blocks in the South Kona landslide, Hawaii, *Geology*, 23, 125-128, 1995.

Morgan, J. K., G. F. Moore, D. J. Hills, and S. Leslie, Overthrusting and sediment accretion along Kilauea mobile south flank, Hawaii: Evidence for volcanic spreading from marine seismic reflection data, *Geology*, 28, 667-670, 2000.

Nakamura, K., Why do long rift zones develop in Hawaiian volcanoes--A possible role of thick oceanic sediments, *Bull. Volcanol. Soc. Jpn*, 25, 255-269, 1980.

Nettles, M., and G. Ekstrom, Faulting mechanism of anomalous earthquakes near Bardarbunga Volcano, Iceland, *J. Geophys. Res.*, 103, 17,973-17,983, 1998.

Okubo, P. G., H. M. Benz, and B. A. Chouet, Imaging the crustal magma sources beneath Mauna Loa and Kilauea Volcanoes, Hawaii, *Geology*, 25, 867-870, 1997.

Owen, S., P. Segall, J. Freymueller, A. Mikilius, R. Denlinger, T. Arnadottir, M. Sako, and R. Burgmann, Rapid deformation of the south flank of Kilauea Volcano, Hawaii, *Science*, 267, 1328-1331, 1995.

Sibson, R. H., Implications of fault valve behavior for rupture nucleation and recurrence, *Tectonophysics*, 211, 283-293, 1992.

Swanson, D. A., A D. Wendell, and R. S. Fiske, Displacement of the south flank of Kilauea volcano. the results of forceful intrusion of magma into the rift zones, *U.S Geol. Prof Pap.*, 963, 39 pp., 1976.

Thurber, C. H , and A. E. Gripp, Flexure and seismicity beneath the south flank of Kilauea volcano and tectonic implications, *J. Geophys Res.*, 93, 4271-4278, 1988.

Walder, J., and A. Nur, Porosity reduction and crustal pore pressure development, *J Geophys Res.*, 89, 11,539-11,548, 1984.

Wallace, M. H., and P. T. Delaney, Deformation of Kilauea volcano during 1982 and 1983: A transition period, *J Geophys Res*, 100, 8201-8219, 1995.

Wyss, M., A proposed source model for the great Kau, Hawaii, earthquake of 1868, *Bull. Seismol Soc. Am.*, 78, 1450-1462, 1988.

Wyss, M., D. Gillard, and B Liang, An estimate of the absolute stress tensor in Kaoiki, Hawaii, *J. Geophys. Res*, 97, 4763-4668, 1992a

Wyss, M., B. Liang, W. R. Tanigawa, and X. Wu, Comparison of orientation of stress and strain tensors based on fault plane solutions in Kaoiki, Hawaii, *J. Geophys. Res.*, 97, 4769-4790, 1992b.

Yang, X., P. M. Davis, and J. H. Dieterich, Deformation from inflation of a dipping finite prolate spheroid in an elastic half-space as a model for volcanic stressing, *J. Geophys Res*, 93, 4249-4257, 1988.

Yang, X., P M. Davis, P. T. Delaney, and A T. Okamura, Geodetic analysis of dike intrusion and motion of the magma reservoir beneath the summit of Kilauea Volcano, Hawaii: 1970-1985, *J. Geophys. Res.*, 97, 3305-3324, 1992.

Yin, A., Mechanics of wedge-shaped fault blocks, 1, An elastic solution for compressional wedges, *J Geophys. Res.*, 98, 14,245-14,256, 1993.

Yin, A., and T. K. Kelty, Structural evolution of the Lewis plate in Glacier National Park, Montana: Implications for regional tectonic development, *Geol. Soc. Am. Bull.*, 103, 1073-1089, 1991.

T.K. Kelty and A. Yin, Department of Earth and Space Sciences, University of California, 3806 Geology Building, Los Angeles, CA 90095-1567. (yin@ess.ucla.edu)